15. PALEOLATITUDE INFERRED FROM CRETACEOUS SEDIMENTARY AND IGNEOUS CORES RECOVERED FROM LEG 210, NEWFOUNDLAND MARGIN[1]

Xixi Zhao,[2] Bruno Galbrun,[3] Heike Delius,[4] and Qingsong Liu[5]

ABSTRACT

We conducted an integrated paleomagnetic and rock magnetic study on cores recovered from Ocean Drilling Program Sites 1276 and 1277 of the Newfoundland Basin. Stable components of magnetization are determined from Cretaceous-aged sedimentary and basement cores after detailed thermal and alternating-field demagnetization. Results from a series of rock magnetic measurements corroborate the demagnetization behavior and show that titanomagnetites are the main magnetic carrier. In view of the normal polarity of magnetization and radiometric dates for the sills at Site 1276 (~98 and ~105 Ma, both within the Cretaceous Normal Superchron) and for a gabbro intrusion in peridotite at Site 1277 (~126 Ma, Chron M1), our results suggest that the primary magnetization of the Cretaceous rocks is likely retained in these rocks. The overall magnetic inclination of lithologic Unit 2 in Hole 1277A between 143 and 180 meters below seafloor is 38°, implying significant (~35° counterclockwise, viewed to the north) rotation of the basement around a horizontal axis parallel to the rift axis (010°). The paleomagnetic rotational estimates should help refine models for the tectonic evolution of the basement. The mean inclinations for Sites 1276 and 1277 rocks imply paleolatitudes of 30.3° ± 5.1° and 22.9° ± 12.0°, respectively, with the latter presumably influenced by tectonic rotation. These values are consistent with those inferred from the mid-Cretaceous reference poles for North America, suggesting that the inclination determinations are reliable and consistent with a drill site on a location

[2]Center for Study of Imaging and Dynamics of the Earth, Institute of Geophysics and Planetary Physics, University of California, Santa Cruz CA 95064, USA.
xzhao@pmc.ucsc.edu
[3]Département de Géologie Sédimentaire, Université Paris VI, 75252 Paris Cedex 5, France.
[4]Department of Geology, University of Leicester, University Road, Leicester LE1 7RH, United Kingdom.
[5]School of Ocean and Earth Science, University of Southampton, National Oceanography Centre, European Way, Southampton SO14 3ZH, United Kingdom.

in the North America plate since at least the mid-Cretaceous. The combined paleolatitude results from Leg 210 sites indicate that the Newfoundland Basin was some 1800 km south of its current position in the mid-Cretaceous. Assuming a constant rate of motion, the paleolatitude data would suggest a rate of 12.1 mm/yr for the interval from ~130 Ma (Site 1276 age) to present, and 19.6 mm/yr for the interval from 126 Ma (Site 1277 age) to recent. The paleolatitude and rotational data from this study are consistent with the possibility that Site 1276 may have passed over the Canary and Madeira hotspots that formed the Newfoundland Seamounts in the mid-Cretaceous.

INTRODUCTION

The mid-Cretaceous (124–84 Ma) was a period of unrest in geologic history. In the mid-Cretaceous, the breakup of the supercontinent Gondwana into separate continents was still under way, which caused the rift between South America and Africa (Van der Voo, 1993). Geological evidence points toward an unusually high rate of volcanic activity in the mid-Cretaceous (Larson, 1991). Crustal-growth events termed "large igneous provinces" (LIPs) made very important contributions to the lithosphere during the mid-Cretaceous (Eldholm and Coffin, 2000). Several large LIPs in the world such as the Ontong Java Plateau (120 Ma) (Neal et al., 1997; Mahoney and Coffin, 1997), the main portion of the Kerguelen Plateau (115–80 Ma) (Coffin, Frey, Wallace, et al., 2000), the Madagascar LIP (84–91 Ma) (Storey et al., 1997), the High Arctic LIP (85–95 Ma) (Brinkman and Tarduno, 2005), and the Caribbean LIP (87–90 Ma) (Kerr et al., 1997) were formed during this time. This global magmatism is marked as well by increases in production of oceanic plateaus and seamount chains, such as the Newfoundland Seamounts (97.7 Ma) (Sullivan and Keen, 1977) (Fig. F1). A key piece in this mid-Cretaceous geologic puzzle is the Cretaceous Normal Superchron (CNS), a period during which Earth's magnetic field was so uncharacteristically steady that it did not switch from normal to reversed polarity for ~40 m.y. (Aptian–Santonian, 124–84 Ma on the geologic timescale of Gradstein et al., 2004, used here). These geological and geophysical signals in the mid-Cretaceous have excited high interest in the geoscience community, leading many to suggest a connection between all of these phenomena and deep-mantle convection (e.g., Vogt, 1975; Larson and Kincaid, 1996; Besse and Courtillot, 2002).

Several interpretations suggest that North Atlantic extension between North America and Europe continued throughout the entire Early Cretaceous into Aptian time (mid-Cretaceous) (see Tucholke et al., in press, for a thorough discussion). The Atlantic Ocean is still expanding today. Global Positioning System measurements with very long baseline interferometry techniques show that the distance between Onsala (Sweden) and Westford (Massachusetts, USA) is widening by 13.4 ± 0.7 mm/yr (Van der Voo, 1993). The original plate tectonic setting (paleolatitude) and the rate of relative plate motion over the interval of the mid-Cretaceous are, however, largely unconstrained. The Newfoundland-Iberia rift lies between North America and European plates and is a key location to examine these questions.

During Ocean Drilling Program (ODP) Leg 210, two sites (Sites 1276 and 1277) were drilled in the central Newfoundland Basin (Fig. F1). The drill sites are in the transition zone between known continental crust to the west and apparent ocean crust to the east, as identified by magnetic

F1. Bathymetric map of the North Atlantic Ocean, p. 18.
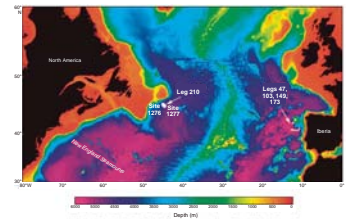
Anomalies M3–M0 (Barremian–Aptian; 129–125 Ma), and they are along a transect exactly conjugate to the ODP Leg 149/173 drilling sites on the Iberia margin. Extensive geophysical work and deep-sea drilling have shown that the transition zone on the conjugate Iberia margin is exhumed continental mantle that is strongly serpentinized in its upper part (Whitmarsh, Sawyer, Klaus, and Masson, 1996). Transition zone crust on the Newfoundland side, however, is typically a kilometer or more shallower and has much smoother topography (Tucholke and Sibuet, 2003). Major goals of Leg 210 were to investigate these differences and to better understand the rifting history by sampling basement and a strong basinwide reflection (U) overlying basement. Recovered rocks from Leg 210 include Cretaceous-age claystone, black shale, sills, basalts, and serpentinized peridotites (Tucholke, Sibuet, Klaus, et al., 2004).

Here we present results from paleomagnetic and rock magnetic measurements from Sites 1276 and 1277, including both Cretaceous sedimentary and igneous rocks. We first describe the results and focus on the cores that provided the most readily interpretable data. We then summarize the data and assess the origin and stability of remanent magnetization. The data are used to establish the paleolatitudes of the Newfoundland Basin during the mid-Cretaceous and to assess possible tectonic rotation of the basement ridge drilled at Site 1277. The paleolatitude constraints are used to infer tectonic drift of the region.

SITE SETTING, LITHOLOGY, SEDIMENTATION RATES, AND AGES

The site locations (Fig. F1) and drilling results are documented in detail in the site chapters of the Leg 210 *Initial Reports* volume and other appropriate papers (see Tucholke, Sibuet, Klaus, et al., 2004; Karner and Shillington, 2005; Tucholke et al., in press). We briefly note the geologic setting, lithology, and core ages of the drill sites here, restricted to Cretaceous-aged rocks.

At Site 1276, we drilled from 800 to 1737 meters below seafloor (mbsf) with excellent recovery throughout the entire cored interval (Tucholke, Sibuet, Klaus, et al., 2004). Five lithologic units are recognized that range from uppermost Aptian–lowermost Albian to lower Oligocene sediments (see fig. F18 in Shipboard Scientific Party, 2004a). Both calcareous nannofossils and planktonic foraminifers provided biostratigraphic control for most of the Site 1276 sections. Based on first and last occurrence datums of microfossils, an age-depth model for Site 1276 was constructed (see fig. F141 in Shipboard Scientific Party, 2004b). The age-depth plot reveals a number of marked changes in sedimentation rate; at least one, and possibly two, unconformities; and two condensed intervals. The changes in slope correspond closely to lithologic unit boundaries. The Cretaceous sedimentary successions are confined to lithologic Units 4 and 5 (see fig. F6 in Shipboard Scientific Party, 2004b). Sediments in Unit 4 are mainly sandy mudstones and muddy sandstones that accumulated slowly (~2 m/m.y.) during Campanian–middle Turonian time (Shipboard Scientific Party, 2004b). The characteristic color of Unit 4 is moderate brown, which is perhaps related to the presence of fine-grained iron oxides (Shipboard Scientific Party, 2004b). Sedimentary cores from Unit 5 are lower Turonian to Albian–uppermost Aptian claystone and mudstone. Finely laminated

X. Zhao et al.
Paleolatitude Inferred from Cretaceous Cores

4

claystones (black shales) are well developed and numerous throughout Unit 5 (fig. F6 in Shipboard Scientific Party, 2004b). Unit 5 accumulated at relatively rapid rates of 15–100 m/m.y., with higher rates downhole. Subunit 5A is dominated by graded sandstone, siltstone, and mudstone intervals that were rapidly emplaced from gravity flows plus very burrowed olive-gray hemipelagic sediment. In contrast, Subunit 5B is composed of mainly burrowed hemipelagic sediments. Subunit 5B includes very finely laminated, calcareous, carbon-rich sediments (black shales). Subunit 5C, like Subunit 5A, is dominated by thick to very thick, gray to greenish black gravity-flow deposits with little true hemipelagic sediment. Subunit 5C is intruded by two major diabase sills, the shallower of which is at a depth equivalent to the "U reflection," a bright horizontal reflection that overlies transitional crust throughout the Newfoundland Basin (fig. F6 in Shipboard Scientific Party, 2004b). Lithologic features of sedimentary contacts with the sill show that the sills were intruded at shallow levels within highly porous sediments. Hydrothermal alteration in the sills ranges from high to complete at the margins to moderate toward the centers (Tucholke, Sibuet, Klaus, et al., 2004). The upper sill (Subunit 5C1) extends from 1612.72 to 1623.00 mbsf (Section 210-1276A-87R-6, 72 cm, to Section 88R-7, 117 cm) (Tucholke, Sibuet, Klaus, et al., 2004). The rocks are aphanitic to fine-grained aphyric diabase. The upper sill is ~10 m thick and preserves chilled margins at its upper and lower contacts. The sediments show a baked contact at the top of the sill, which is well preserved in Section 210-1276A-87R-6. The lower contact of the sill was not recovered and no baked contact is preserved in the underlying sediments. The lower sill (Subunit 5C2) is an igneous complex extending from Sections 210-1276A-97R-3 to 102R-1 at the base of the hole. The rocks forming the sill complex are aphanitic to medium-grained aphyric to seriate diabase, which are observed in five intervals (intervals 210-1276A-97R-3, 141–150 cm; 97R-4, 0–3 cm; 98R-1, 112–137 cm; 98R-2, 1–31 cm; and from 98R-CC, 10 cm, to the last recovery in 102R-1, 0–2 cm [see Shipboard Scientific Party, 2004b]). In the first four intervals, the sills range in thickness from decimeters to a few centimeters; the thinner sills may represent small apophysies (magmatic fingers) related to the larger sills. From Core 210-1276A-98R to the base of the hole, low recovery and strong drilling disturbance make it difficult to determine if this complex is a single thick sill or several thinner sills. The age-depth plot for Site 1276 suggests that the host sediments for the upper and lower sills are lower Albian–uppermost Aptian (see fig. F141 in Shipboard Scientific Party, 2004b). The ^{40}Ar-^{39}Ar ages of two samples (Samples 210-1276A-88R-2, 88–92 cm, and 88R-3, 76–80 cm) from the upper sill (Subunit 5C1) are 104.7 ± 1.7 Ma and 105.9 ± 1.8 Ma (Hart and Blusztajn, in press). The age of the upper sill emplacement is also independently estimated to be 99.9–105.2 Ma by porosity-age curves (Karner and Shillington, 2005). Excellent ^{40}Ar-^{39}Ar radiometric results from two lower sill (Subunit 5C2) samples (Samples 210-1276A-99R-3, 19–22 cm, and 99R-6, 24–30 cm) yield ages of 95.9 ± 2.0 Ma and 99.7 ± 1.8 Ma, respectively (Hart and Blusztajn, in press). Thus, the sills are substantially younger than the presumed age of the seafloor at Site 1276 (~130 Ma) and are also younger than the host sediments (110–112 Ma). Paleomagnetic samples used in this study are mainly from Unit 5.

Site 1277 is located about 40 km southeast of Site 1276, near magnetic Anomaly M1 on crust that may be oceanic (Shillington et al., 2004, Van Avendonk et al., 2006). Leg 210 drilled Site 1277 to test the inference that the site location was on an oceanic crust formed by early

seafloor spreading in the Newfoundland Basin. However, because of the time constraints for the final operation of the leg, only two units were cored at Site 1277 from 103.9 to 180.3 mbsf (see Shipboard Scientific Party, 2004a). The upper ~57 m of recovered basement (Unit 1) is a sedimentary and volcanic succession, with at least three basaltic flows separated by volcaniclastic and ferruginous sedimentary interbeds (see fig. F2 in Shipboard Scientific Party, 2004c). Variably deformed gabbroic rocks and coarse breccia containing clasts of gabbro and serpentinite are also recovered from this unit. In contrast, the bottom ~38 m consists entirely of variably foliated serpentinized peridotites (fig. F2 in Shipboard Scientific Party, 2004c). These yellow- and green-colored serpentinized peridotites (tectonized harzburgite and serpentinite mylonite) are all cut pervasively by several stages of veining and mineral precipitation. The serpentinized peridotite drilled at Site 1277 is interpreted to be basement that represents tectonically exhumed mantle. This interpretation is compatible with the observation that the serpentinite in Unit 2 shows pervasive brittle deformation and hydrothermal alteration that decreases downhole (Tucholke, Sibuet, Klaus, et al., 2004). The downhole decrease in alteration may explain increasing core recovery with depth, from <9.28% at the top of the serpentinite (Core 210-1277A-6R) to 105.73% at the bottom of the hole (Core 210-1277A-9R, the last core of ODP). An ^{40}Ar-^{39}Ar age of biotite from a gabbro intrusion in peridotite sample from Site 1277 (Sample 210-1277A-9R-1, 20–23 cm) yields an age of 126.5 ± 0.1 Ma (Jagoutz et al., submitted [N1]), which is compatible with a seafloor spreading age (about Anomaly M1, 126 Ma on the geologic timescale of Gradstein et al., 2004).

MAGNETIC MEASUREMENTS, DATA ANALYSIS, AND RESULTS

The paleomagnetic data presented in this paper are of two different types: (1) those obtained using the shipboard pass-through cryogenic magnetometer and (2) those derived from analysis of discrete samples both on the ship and on shore. In order to more fully understand the nature and origin of the remanence carriers within the Cretaceous rocks, supplementary rock magnetic and petrologic characterization of selected samples were also performed at University of California Santa Cruz, University of Minnesota, and University of Leicester. Data from different laboratories are found to be in excellent agreement with each other. The data include shipboard split-core data that are available in the ODP database but were not archived in the Leg 210 *Initial Reports* volume, as well as data collected since Leg 210 (Table T1). Table T2 summarizes the rock magnetic results of this study. Below, we outline the laboratory measurement procedure and data analysis methods and describe the data.

Split-Core Results from Shipboard Measurements

The laboratory procedure and results of shipboard paleomagnetic measurements are described in detail in the site chapters of Tucholke, Sibuet, Klaus, et al. (2004). Briefly, magnetic measurements were performed by passing continuous archive-half core sections of the split cores through a 2G cryogenic magnetometer. Remanence measurements were made at 2-cm intervals on all archive-half core pieces

longer than ~6 cm. Typically, archive-half cores were subjected to step-wise alternating-field (AF) demagnetization at 5- to 10-mT steps up to maximum peak fields of 60 mT. The characteristic remanent magnetization (ChRM) directions were calculated by principal component analysis (Kirschvink, 1980) at all measurement points along the core pieces where stable vector components could be identified on vector demagnetization plots (Zijderveld, 1967).

Split-core paleomagnetic data obtained at Sites 1276 and 1277 exhibit considerable variations in demagnetization behavior among various lithologies. A remagnetization imparted by the coring process is commonly encountered, as observed in many previous legs (e.g., Ade-Hall and Johnson, 1976; Gee et al., 1989; Zhao et al., 1994). This remagnetization is characterized by natural remanent magnetization (NRM) inclinations that are strongly biased toward a vertical value (+90) in most cores. In most cases, the drilling overprint can be removed with 10- to 30-mT AF demagnetization, and the ChRM direction can be isolated using stepwise demagnetization at higher fields. The effect of removal of this overprint by AF cleaning is a significant decrease in intensity and a shift toward shallower inclination. Examples of good-quality AF demagnetization results are shown in Figure F2. As shown in Figure F2, marble Sample 210-1276A-87R-6, 62 cm, from just above the sill of Subunit 5C1, has the same ChRM inclination as the thermally altered meta-grainstone Sample 210-1276A-87R-6, 72 cm, from sediments contacting the chilled margin of the upper diabase sill, indicating they acquired primary magnetization during the intrusion of the sill.

Sandy mudstones and muddy sandstones in Unit 4 of Site 1276 have a mean NRM intensity of 3×10^{-2} A/m and magnetic susceptibility of 1×10^{-4} SI units. A strong drilling-induced overprint is present throughout Unit 4, which severely limits paleomagnetic work. Sedimentary cores from Unit 5 have lower NRM intensity (mean ~2.5×10^{-3} A/m) and magnetic susceptibility (mean ~8×10^{-5} SI units). The magnetization of dark claystones (black shale) is typically an order of magnitude (in some cases even two orders) weaker than the light-colored sediments. Nevertheless, the ChRM directions can still be defined from these black shales using stepwise demagnetization.

For the two diabase sills of Site 1276, we performed detailed AF demagnetization on all coherent pieces that could be oriented unambiguously with respect to the top of the core. For a majority of the cases, the ChRM direction can be isolated at higher AF fields (e.g., Fig. F3). The inclinations of the ChRM direction for these two diabase sills are all positive. Although the NRM intensities and inclinations are quite variable, we identified distinct differences between the upper and lower diabase sills. The lower sill (Sections 210-1276A-99R-1 to 99R-6; ~1719–1725 mbsf) is generally more weakly magnetized; the average intensity and magnetic susceptibility are 0.8 A/m and 3.2×10^{-3} SI units, respectively. The upper sill (Sections 210-1276A-87R-6 through 88R-7; ~1613–1623 mbsf), however, is more magnetic and has average intensity and magnetic susceptibility values consistently above 3.8 A/m and 5.6×10^{-2} SI units, respectively. The average Königsberger ratio Q (defined as the ratio of the NRM intensity to the induced magnetization in the local Earth's field) for the upper sill is ~1.9, whereas Q values in the lower sill have a mean of 9.5.

Paleomagnetic data obtained by pass-through cryogenic magnetometer measurements for Site 1277 indicate that the greenish gabbro cataclasite in Core 210-1277A-2R has the lowest NRM intensity (~0.02–0.3

F2. AF demagnetization for split-core samples, p. 19.
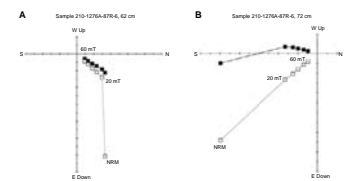
F3. AF demagnetization for diabase sills, p. 20.
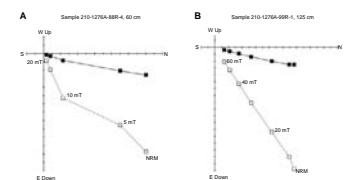
A/m) compared with relatively fresh aphyric basalt in Cores 210-1277A-1R, 3R, and 5R (~1–4 A/m), gabbro at the base of Core 210-1277A-4R and in the lower part of Core 210-1277A-5R (~0.2–0.5 A/m), and serpentinized peridotites in Core 210-1277A-9R (1–9 A/m). It is encouraging to note that a basaltic sample (Sample 210-1277A-1W-2, 28 cm) and adjacent sediment (Sample 210-1277A-1W-2, 94 cm) have the same stable inclination values (Table T1). The green breccia, on the other hand, displayed variable inclinations, which is consistent with the expectation that the breccia is unsorted and there should be a great variation in inclinations of the clasts. This observation suggests that there was no thermal or other event that completely remagnetized both breccia and basalts. Shipboard observation suggests that rocks in Unit 1 are largely allochthonous. The consistent ChRM inclinations in the basalt and sediments, however, suggest that they might have been deposited in situ. The serpentine peridotites in Core 210-1277A-9R showed a variable degree of overprinting, but AF demagnetization easily removed the overprinting and isolated the ChRM direction. ChRM inclinations obtained from different parts of long, coherent pieces generally agree within a few degrees and cluster around a mean of 40°, which is in general agreement with inclinations from the basalt, gabbro, and sediments in Unit 1.

Although many of the data from the shipboard pass-through measurements probably contain valid estimates of the ChRM of sedimentary and igneous rocks (Fig. F4), assessing which intervals are accurate recorders is not always easy because of the presence of the drilling remagnetization, coring disturbance, and possible inclination shallowing because of compaction, tectonic rotation, or both. Nevertheless, shipboard data do provide a framework for the identification of specific intervals where more extensive shore-based paleomagnetic analyses are required. The higher resolution of the split-core data (compared with minicore data) is also useful in assessing the independence of stratigraphically adjacent igneous units in sampling geomagnetic secular variation.

In order to obtain reliable estimates of the ChRM from the split-core data of sedimentary and igneous rocks, we devised several criteria to avoid overprinted and magnetically unstable intervals. Our criteria included

1. Rejecting any measurements with inclination steeper than ±65°, a very likely sign that the drilling-induced remagnetization is still present;
2. Accepting samples with principal component maximum angular deviation angles <10°; and
3. Rejecting samples with inclinations less than ±10°, whose magnetization was likely affected by inclination shallowing, paleosecular variation, tilt of drill holes, and/or tectonic rotations.

We generally accept data where there is agreement between the split-core and discrete inclinations from a similar interval (Table T1). A total of 178 split-core paleomagnetic determinations satisfy the above-mentioned acceptance criteria for further analyses and paleolatitude estimates.

AF and Thermal Demagnetization of Discrete Samples

Discrete paleomagnetic samples were used for both shipboard and shore-based paleomagnetic studies. These 2.5-cm cylindrical samples

F4. AF and thermal demagnetization for samples, p. 21.
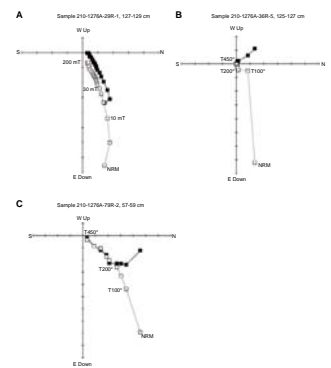
were drilled from core sections that contained long pieces and generally were taken from the least-altered parts. In all cases, the uphole direction was recorded on the sample by means of an orientation arrow before removal from the core section. All samples were kept in a low-field environment (field-free room) to prevent viscous remanence acquisition; the NRM intensity or direction of the minicore samples did not change significantly (<5%) after zero-field storage for 2 weeks. Samples were then stepwise AF or thermally demagnetized. During thermal demagnetization, the initial susceptibility was monitored between each temperature step as a means of assessing any irreversible mineralogical changes associated with heating. Apart from small insignificant fluctuations, the susceptibility of minicore samples generally did not change until after they had been heated to 350°C. Above this temperature, many samples showed a decrease or increase in susceptibility and some samples exhibited unstable demagnetization behavior.

Whenever possible, demagnetization was continued until an unambiguous and reliable determination of the stable component of magnetization had been achieved. As with the long core pieces, a vector diagram was used for each minicore sample to identify the magnetic components of magnetization that were present. For samples that gave reliable demagnetization results, magnetic components were determined by fitting least-squares lines to segments of the vector demagnetization plots (Kirschvink, 1980) that were linear in three-dimensional space. Figure F4 illustrates the demagnetization behavior of several samples from different lithologic units. These samples demonstrate the removal of the vertically directed drilling-induced magnetization component and the isolation of a stable component that is univectorially decaying toward the origin of the vector plots (Zijderveld, 1967). These demagnetization behaviors are typical of the majority of samples in this study. A significant number of samples from the upper sill of Site 1276 maintained much steeper inclination values after progressive demagnetization, which may be because of an overprint that has not been completely removed or because of paleosecular variation. In contrast, the magnetization of the lower sill samples is quite stable and well behaved. A small, random component of magnetization was easily removed by demagnetization and the characteristic component quickly revealed itself. Mean ChRM inclination of the lower sill is ~50°, which is similar to inclinations of sediments above the sill.

We always define the ChRM direction based on the higher temperature or AF demagnetization steps. We used the same criteria by which we accepted the split-core data, namely, excluding those samples with inclinations greater than ±65° or less than ±10° from the mean calculation. In addition, we also rejected demagnetization results from samples that altered significantly during thermal cleaning (those marked unstable in Table T1). A total of 106 minicore data are accepted data. The combined data sets are plotted against depth in Figures F5 and F6.

Rock Magnetic Characterization

In order to more fully understand the nature and origin of the remanence carriers within the Cretaceous rocks, supplementary rock magnetic characterization of selected discrete samples was performed at the paleomagnetism laboratories at University of California Santa Cruz and at the Institute for Rock Magnetism of the University of Minnesota. A total of 32 samples were subjected to a wide range of rock magnetic measurements, including

F5. Downhole variation in ChRM inclinations, Site 1276, p. 22.
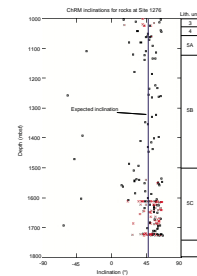
F6. Downhole variation in ChRM inclinations, Site 1277, p. 23.
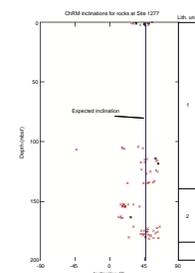
1. Curie temperature determinations using both low and high applied fields (0.05 mT and 1 T, respectively);
2. Hysteresis loop parameter measurements: saturation magnetization (J_s), saturation remanence (J_r), coercivity (B_c), and remanent coercivity (B_{cr}) determined from 10 to 400 K; and
3. Saturation isothermal remanent magnetization as a function of temperature (10–300 K).

Transitions in the magnetic properties of magnetite, pyrrhotite, and hematite occur at low temperatures and they provide a potential means of magnetic mineral identification. Magnetite exhibits a crystallographic phase transition from cubic to monoclinic at 110–120 K, known as the Verwey transition (Verwey et al., 1947).

As summarized in Table T2, the diabase sill samples of Site 1276 are uniformly characterized by a single magnetic phase with Curie temperatures between 515°C and 580°C (Table T2), compatible with Ti-poor magnetite. They also display quite uniform low-temperature properties, with distinct Verwey transition temperatures ~120 K and show similar hysteresis properties that are compatible with pseudosingle domain (PSD) particles, with intermediate grain sizes (0.08–9 μm). These results are consistent with those of Fe-Ti oxide analysis on Leg 210 cores (H. Delius, pers. comm., 2007), which suggests that titanomagnetite and ilmenite are the two dominant minerals in the sill samples.

Curie temperature measurements on the brown dunite samples in Hole 1277A display a significant drop of magnetic moment around 420°C (Fig. F7A), most likely attributable to the presence of maghemite. The low-temperature curves for the yellow-brown colored peridotites did not show any Verwey transition (Fig. F7B), suggesting that the magnetic carrier in these samples is not magnetite. In contrast, the dark-colored peridotite samples exhibit a strong Verwey transition in the vicinity of 110 K (Fig. F7D), which is indicative of the presence of titanomagnetite. The Curie temperatures for these dark-colored peridotites are between 550°C and 580°C, suggesting that titanomagnetite is the magnetic carrier (Fig. F7C). The thermomagnetic curves of these samples exhibit very little difference between heating and cooling of the samples, signifying that the magnetite underwent no chemical alteration during heating. Room-temperature hysteresis parameters further indicate that the magnetites in the serpentinized peridotite samples are predominantly PSD grains (Fig. F8).

Taken together, the rock magnetic properties corroborate the demagnetization behavior and suggest that the igneous rocks in Sites 1276 and 1277 are probably good paleomagnetic recorders that can preserve original magnetization. The generally good magnetic stability exhibited by these titanomagnetite-bearing rocks suggests that their stable inclinations (and corresponding paleolatitudes) may be reliable for tectonic reconstructions.

Age of Magnetization

Determining the age of magnetization is absolutely critical and often not always straightforward. This has been a challenging problem in paleomagnetic research on ODP core materials. The directions associated with the ChRM in the two diabase sills in Site 1276 displayed high consistency and were isolated after removal of a secondary overprint, leading us to interpret them as primary. The agreement between the split-core data and discrete inclinations from the same intervals is ex-

F7. Temperature dependence of magnetization curves, p. 24.
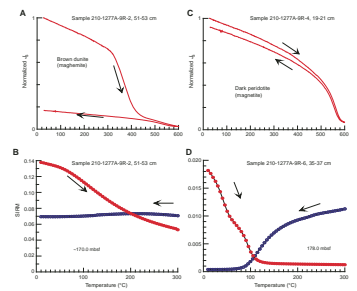
F8. Hysteresis ratios plotted on a Day-type diagram, p. 25.
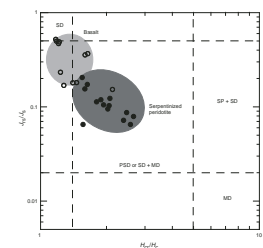
cellent. Thus, the split-core data from sill cores also provide accurate estimates of the ChRM inclinations. The inclinations of the ChRM direction for these two diabase sills are all positive. The simplest explanation of the positive inclinations is that they represent normal polarity magnetization, probably acquired within the CNS (84–124 Ma). Indeed, the radiometric ages indicate that the two sills were emplaced at ~98 Ma and ~105 Ma (Hart and Blusztajn, in press). Thus, the normal polarity observed in the sill samples is consistent both with the CNS and the age of the rocks. The biostratigraphic ages for sedimentary successions in Units 4 and 5 are Albian–Santonian, which is also within the CNS. Cores in Units 4 and 5 are mostly normally magnetized (>97% of the selected data). This normal polarity is consistent with magnetization that should have been acquired during the CNS. In view of the normal polarity and inclination values of magnetization identified from the sill samples, the ChRM of sediments is probably within the broad age of the CNS as well.

At Site 1277, the magnetically cleaned inclinations in the basalts (Unit 1) and serpentinized peridotites (Unit 2) are systematically shallower than the inclination expected today (64°) at the drill site, indicating that the ChRM is not a recent overprint. The similar inclination values observed in basalt, sedimentary interbeds, and peridotites (excepting significantly different inclination from the chaotic breccias) are necessary but not sufficient proof that the stable magnetization recorded by these rocks is original. The available radiometric age (126.5 Ma) of gabbro in the Site 1277 peridotites puts direct age constraints on the magnetization. The mean ChRM inclinations are statistically indistinguishable from the inclinations of rocks from Site 1276 and also are compatible with shallow inclinations observed at ODP Leg 173 sites on the conjugate margin (Zhao, 2001), leading us to believe that the characteristic components can be regarded as recorders of the paleofield sometime in the Cretaceous. As described below, the estimated paleolatitudes from the mean inclinations observed in both Units 1 and 2 are in agreement with the expected Cretaceous paleolatitudes for both Iberia and North America. For all of these reasons, plus the straightforward demagnetization behavior, we believe that the mean inclination from Site 1277 is plausible, and even likely, near primary magnetization acquired when the rocks were formed.

Paleosecular Variation

Before the paleomagnetic data can be converted to paleolatitudes for paleogeographic reconstructions, it is important to ensure that paleosecular variation has been averaged out so that the mean inclination represents a time-averaged geocentric axial dipole field. For Site 1276, sedimentation rates are generally low (~2 m/m.y. for sedimentary rocks in Unit 4 and 15–100 m/m.y. for sediments in Unit 5); thus, the inclination from a single sample represents a partially time-averaged geomagnetic field and samples spanning a depth interval of 2–50 m should be sufficient to average secular variation.

Igneous samples from a single cooling unit only give an instantaneous measure of the geomagnetic field. The time interval between cooling units is rarely known. The number of independent units, however, can be estimated from the pattern and differences among flow means (Cox and Gordon, 1984; Sager, 2006). If the difference between flow means is small (less than ~10), then these means are considered correlated and should be averaged. Tarduno and Cottrell (1997) and Ac-

X. Zhao et al.
Paleolatitude Inferred from Cretaceous Cores

11

ton et al. (2000) have suggested that generally more than ~10 independent cooling units are considered sufficient to average secular variation. In this regard, the numbers of cooling units represented by the three basalt flows of Unit 1 at Site 1277 as well as the upper sill (Subunit 5C1) at Site 1276 certainly are not large enough to ensure averaging of secular variation. It is also difficult to ascertain whether the paleosecular variation has been fully averaged from the lower sill complex of Site 1276 and the serpentinized peridotites at Site 1277. However, we note that for each sill unit in Hole 1276A, the mean inclinations of sill samples are statistically indistinguishable from those of overlying Cretaceous sediments, both baked and unbaked. This observation is perhaps the most compelling argument for isolating the primary ChRM that may represent a time-averaged field, although this observation is not sufficient by itself.

Paleolatitude

Assuming that the inclination represents the primary remanence at the time when these rocks were formed, the inclination of the time-averaged magnetic field recorded in Leg 210 rocks can be used to calculate the paleolatitude at which the rocks were formed. We have taken the absolute value of inclinations and employed the technique developed by McFadden and Reid (1982) to estimate true mean inclinations from our core data. This technique tracks the statistical significance of inclination clustering and allows us to estimate Fisher means (Fisher, 1953) and confidence limits over given time intervals. We obtained a mean Site 1276 inclination of 46.3° (α95 = 7.3°, k = 78.6, N = 7) using estimated average inclinations from the seven mean inclination groups (Table T3). If all samples are treated as independent readings, we obtain a statistically indistinguishable mean inclination of 49.4° (α95 = 2.8°, k = 19.0, N = 193), suggesting that the mean Site 1276 inclination is very robust. For Site 1277 samples, we have calculated the grand mean with three different methods (Table T3). The means computed differ little among these methods, but we prefer to use the mean inclination of 38.5° (α95 = 17.6°, k = 13.8, N = 7) averaged by mean inclination of the drill cores, as the associated uncertainties may be more representative of the true values. Using the mean inclinations for Sites 1276 and 1277 (italic data in Table T3), we have calculated paleolatitudes for the Newfoundland drill sites. The Site 1276 rocks imply a paleolatitude of 30.3° with 95% confidence limits (α95) of approximately ±5.6°, whereas Site 1277 rocks yield a paleolatitude of 22.9° with α95 of ±12.0° (Table T3).

T3. Mean inclinations and paleolatitudes, p. 35.

DISCUSSION

The generally good magnetic stability and other properties exhibited by the diabase sills of Site 1276 support the inference that the characteristic directions of magnetization isolated from these rocks were acquired during the CNS. This interpretation is compatible with radiometric age dates. The stable inclinations identified from these samples are therefore useful for plate tectonic studies.

At Site 1277, the rock magnetic results of serpentinized peridotites give important information about the origin of remanence and the magnetic minerals present in the cores. Dark-colored peridotites with Ti-poor titanomagnetite exhibit a strong Verwey transition in the vicinity of 110 K with hysteresis ratios suggesting that the bulk magnetic

grain size is in the PSD range. Therefore, the dark-colored peridotites are most likely good paleomagnetic recorders and probably have preserved original and stable magnetic remanences. Similar inclination values observed in basalt, sedimentary interbeds, and peridotites (excepting different inclinations from breccias) are necessary but not sufficient proof that the stable magnetization recorded by these rocks is original. However, the mean inclinations of these samples are close to the theoretically predicted values for the paleolatitude of the drilling sites, indicating that they may represent primary magnetization. Available age data constrain the magnetization (and hence, paleolatitude) to have been acquired in the Cretaceous.

The Cretaceous apparent polar wander path for North America is well determined, and its reference paleopoles can be used to predict paleomagnetic directions for a given age at a given site (Van der Voo, 1993). In order to compare our paleomagnetic inclination data with other North American data, it is necessary to transform the results into pole space. Because our data are azimuthally unoriented, we cannot define a paleomagneic pole for Leg 210 drill sites. However, the pole must lie on a small circle centered on the site and with a radius of the paleomagnetic paleocolatitude. As shown in Figure F9, the paleocolatitudes of the two Leg 210 sites are comparable with those inferred from the mid-Cretaceous reference poles for North America (also see Table T4), which is consistent with the Leg 210 sites having resided on the North American plate since the Cretaceous.

Taken together, the paleomagnetic results from Sites 1276 and 1277 give a clear indication of the change of paleolatitude of the Newfoundland Basin since the mid-Cretaceous. The 30.3° ± 5.1° paleolatitude estimated from the Cretaceous sediments and sills implies that Site 1276 has drifted northward 15.1° since ~130 m.y. ago. For Site 1277, although the match of the basalt paleolatitude and the serpentinized peridotites paleolatitude might be fortuitous, the combined paleolatitude of basalt and peridotite suggests that Site 1277 has undergone a 22.3° northward displacement since ~126 Ma. The averaged paleolatitude for Leg 210 sites indicates that the Newfoundland Basin has drifted some 1800 km since the mid-Cretaceous. Assuming a constant rate of motion, the paleolatitude data would suggest a rate of 12.1 mm/yr for the interval from ~130 Ma (Site 1276 age) to present and 19.6 mm/yr for the interval from 126 Ma (Site 1277 age) to recent.

The origin and nature of the Newfoundland transitional crust are still intensively debated. Three tectonic hypotheses have been advanced to explain the crustal structure and rift history of the Newfoundland and Iberia transition zones (see Tucholke, Sibuet, Klaus, et al., 2004), including (1) the transition zone is composed of largely of very slow spreading oceanic crust, (2) the transition zone was formed by extreme extension and mantle exhumation in an amagmatic rift, and (3) the transition zone is strongly thinned continental crust. Although our data do not allow us to discriminate among these hypotheses, the paleomagnetic data do provide constraints for the possible rotation history of the fault block on which Site 1277 was drilled. We performed a simple exercise to find out how much rotation is needed to change the expected Cretaceous inclination to the observed inclination. Small-circle paths of the presumed starting Cretaceous inclination about a specified rotation axis were calculated to find when the inclinations could coincide. The results suggest that the variably foliated serpentinized peridotites in the bottom ~38 m (Unit 2) of Hole 1277A could be rotated counterclockwise (with respect to today's north) up to

F9. Paleocolatitudes for Sites 1276 and 1277, p. 26.
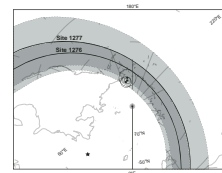
T4. Paleolatitudes obtained from this study, p. 36.

~35° parallel to the rift axis (010°) without exceeding the bounds of the observed inclination. Thus, it seems clear that significant rotations are acceptable for at least some of the data from Site 1277. Given that Sites 1276 and 1277 are presently separated by 0.20° latitude, tectonic rotation at Site 1277 may best explain the large (7.4°) latitude separation between the sites suggested by the paleomagnetic results. We speculate that the counterclockwise rotations may be associated with the intraplate tensional tectonics prior to the onset of seafloor spreading as proposed in Tucholke et al. (in press).

As mentioned in the "Introduction," p. 2, the mid-Cretaceous was characterized by widespread rifting, continental breakup, and global magmatism. LIP emplacement peaked near mid-Cretaceous time, although there has been no satisfactory explanation as to why this peak occurred. Trachytes from the Newfoundland Seamounts give ages of 97.7 ± 1.5 Ma (Sullivan and Keen, 1977). Thus, it would seem that the ages of emplacement of the two sills at Site 1276 are possibly related to the emplacement of the Newfoundland Seamounts (Karner and Shillington, 2005), and the paleolatitude data from this study are consistent with the possibility that Site 1276 may have passed over the Newfoundland Seamounts hotspot in the mid-Cretaceous. Recent geochemical studies also show that Site 1276 sills are not derived from typical mid-ocean-ridge basalt (asthenoshpheric) upper mantle but are broadly similar to oceanic hotspot basalts (Hart and Blusztajn, in press). Whether the basalt at Site 1277 is also coeval with the Newfoundland hotspot activity is not certain at this time, although the basalt stable inclinations and normal polarities are suggestive that this is so. Radiometric dating of the basalts and future drilling in the Newfoundland Basin are needed to answer such questions.

CONCLUSION

The Cretaceous sedimentary and igneous rocks recovered from Sites 1276 and 1277 preserve a magnetic memory of the mid-Cretaceous geomagnetic field and provide paleolatitudinal constraints for paleogeographic reconstructions. The combined paleolatitude results from Leg 210 sites provide evidence that the Newfoundland Basin was positioned some 1800 km south of its current position in the mid-Cretaceous and then migrated northward to its position today. The paleolatitude data and radiometric dates for the sills at Site 1276 are consistent with the notion that the sills not only reflect significant postrift magmatism but also may have been coeval with Newfoundland Seamount hotspot activity. The overall magnetic inclination of rocks in Hole 1277A between 143 and 180 mbsf allows for significant (~35° counterclockwise) rotation of basement parallel to the rift axis. The paleomagnetic rotational estimates are consistent with the recent proposal that intraplate extension may have occurred during opening of the Newfoundland–Iberia rift (Tucholke et al., in press).

ACKNOWLEDGMENTS

REFERENCES

Acton, G.D., Galbrun, B., and King, J.W., 2000. Paleolatitude of the Caribbean plate since the Late Cretaceous. *In* Leckie, R.M., Sigurdsson, H., Acton, G.D., and Draper, G. (Eds.), *Proc. ODP, Sci. Results,* 165: College Station, TX (Ocean Drilling Program), 149–173. **doi:10.2973/odp.proc.sr.165.001.2000**

Ade-Hall, J.M., and Johnson, H.P., 1976. Paleomagnetism of basalts, Leg 34. *In* Yeats, R.S., Hart, S.R., et al., *Init. Repts. DSDP,* 34: Washington (U.S. Govt. Printing Office), 513–532. **doi:10.2973/dsdp.proc.34.143.1976**

Besse, J., and Courtillot, V., 2002. Apparent and true polar wander and the geometry of the geomagnetic field over the last 200 Myr. *J. Geophys. Res. [Solid Earth Planets],* 107:11. **doi:10.1029/2000JB000050**

Brinkman, D.B., and Tarduno, J.A., 2005. A Late Cretaceous (Turonian–Coniacian) high-latitude turtle assemblage from the Canadian Arctic. *Can. J. Earth Sci.,* 42(12):2073–2080. **doi:10.1139/e05-074**

Coffin, M.F., Frey, F.A., Wallace, P.J., et al., 2000. *Proc. ODP, Init. Repts.,* 183: College Station, TX (Ocean Drilling Program). **doi:10.2973/odp.proc.ir.183.2000**

Cox, A., and Gordon, R.G., 1984. Paleolatitudes determined from paleomagnetic data from vertical cores. *Rev. Geophys. Space Phys.,* 22:47–72.

Day, R., Fuller, M., and Schmidt, V.A., 1977. Hysteresis properties of titanomagnetites: grain-size and compositional dependence. *Phys. Earth Planet. Inter.,* 13(4):260–267. **doi:10.1016/0031-9201(77)90108-X**

Dunlop, D.J., 2002. Theory and application of the Day plot (M_{rs}/M_s versus H_{cr}/H_c), 1. Theoretical curves and tests using titanomagnetite data. *J. Geophys. Res.,* 107(B3):2056. **doi:10.1029/2001JB000486**

Eldholm, O., and Coffin, M.F., 2000. Large igneous provinces and plate tectonics. *In* Richards, M.A., Gordon, R.G., and van der Hilst, R.D. (Eds.), *The History and Dynamics of Global Plate Motions.* Geophys. Monogr., 121:309–326.

Fisher, R.A., 1953. Dispersion on a sphere. *Proc. R. Soc. London, Ser. A,* 217:295–305.

Gee, J., Staudigel, H., and Tauxe, L., 1989. Contribution of induced magnetization to magnetization of seamounts. *Nature (London, U. K.),* 342(6246):170–173. **doi:10.1038/342170a0**

Gradstein, F.M., Ogg, J.G., and Smith, A. (Eds.), 2004. *A Geologic Time Scale 2004:* Cambridge (Cambridge Univ. Press).

Hart, S.R., and Blusztajn, J., in press. Age and geochemistry of the mafic sills, ODP Site 1276, Newfoundland margin. *Geochem. Geol.*

Karner, G.D., and Shillington, D.J., 2005. Basalt sills of the U reflector, Newfoundland Basin: a serendipitous dating technique. *Geology,* 33(12):985–988. **doi:10.1130/G21971.1**

Kerr, A.C., Tarney, J., Marriner, G.F., Nivia, A., and Saunders, A.D., 1997. The Caribbean-Colombian Cretaceous igneous province: the internal anatomy of an oceanic plateau. *In* Mahoney, J.J., and Coffin, M.F. (Eds.), *Large Igneous Provinces: Continental, Oceanic, and Planetary Flood Volcanism.* Geophys. Monogr., 100:123–144.

Kirschvink, J.L., 1980. The least-squares line and plane and the analysis of palaeomagnetic data. *Geophys. J. R. Astron. Soc.,* 62(3):699–718.

Larson, R.L., 1991. Latest pulse of Earth: evidence for a mid-Cretaceous superplume. *Geology,* 19(6):547–550. **doi:10.1130/0091-7613(1991)019<0547:LPOEEF>2.3.CO;2**

Larson, R.L., and Kincaid, C., 1996. Onset of mid-Cretaceous volcanism by elevation of the 670 km thermal boundary layer. *Geology,* 24(6):551–554. **doi:10.1130/0091-7613(1996)024<0551:OOMCVB>2.3.CO;2**

Mahoney, J.J., and Coffin M.F. (Eds.), 1997. Large Igneous Provinces: Continental, Oceanic, and Planetary Flood Volcanism. *Geophys. Monogr.,* 100.

McElhinny, M.W., and McFadden, P.L., 1999. *Paleomagnetism: Continents and Oceans:* San Diego (Academic Press).

McFadden, P.L., and Reid, A.B., 1982. Analysis of paleomagnetic inclination data. *Geophys. J. R. Astron. Soc.,* 69:307–319.

Neal, C.R., Mahoney, J.J., Kroenke, L.W., Duncan, R.A., and Petterson, M.G., 1997. The Ontong Java Plateau. *In* Mahoney, J.J., and Coffin, M.J. (Eds.), *Large Igneous Provinces: Continental, Oceanic, and Planetary Flood Volcanism.* Geophys. Monogr., 100:183–216.

Sager, W.W., 2006. Cretaceous paleomagnetic apparent polar wander path for the Pacific plate calculated from Deep Sea Drilling Project and Ocean Drilling Program basalt cores. *In* Sager, W.W., Acton, G.D., Clement, B.M., and Fuller, M. (Eds.), *ODP Contributions to Paleomagnetism.* Phys. Earth Planet. Int., 156(3–4):329–349. doi:10.1016/j.pepi.2005.09.014

Shillington, D.J., Holbrook, W.S., Tucholke, B.E., Hopper, J.R., Louden, K.E., Larsen, H.C., Van Avendonk, H.J.A., Deemer, S., and Hall, J., 2004. Data report: marine geophysical data on the Newfoundland nonvolcanic rifted margin around SCREECH transect 2. *In* Tucholke, B.E., Sibuet, J.-C., Klaus, A., et al., *Proc. ODP, Init. Repts.,* 210: College Station, TX (Ocean Drilling Program), 1–36. doi:10.2973/odp.proc.ir.210.105.2004

Shipboard Scientific Party, 2004a. Leg 210 summary. *In* Tucholke, B.E., Sibuet, J.-C., Klaus, A., et al., *Proc. ODP, Init. Repts.,* 210: College Station, TX (Ocean Drilling Program), 1–78. doi:10.2973/odp.proc.ir.210.101.2004

Shipboard Scientific Party, 2004b. Site 1276. *In* Tucholke, B.E., Sibuet, J.-C., Klaus, A., et al., *Proc. ODP, Init. Repts.,* 210: College Station, TX (Ocean Drilling Program), 1–358. doi:10.2973/odp.proc.ir.210.103.2004

Shipboard Scientific Party, 2004c. Site 1277. *In* Tucholke, B.E., Sibuet, J.-C., Klaus, A., et al., *Proc. ODP, Init. Repts.,* 210: College Station, TX (Ocean Drilling Program), 1–39. doi:10.2973/odp.proc.ir.210.104.2004

Storey, M., Mahoney, J.J., and Saunders, A.D., 1997. Cretaceous basalts in Madagascar and the transition between plumes and continental lithosphere mantle sources. *In* Mahoney, J.J., and Coffin, M.F. (Eds.), *Large Igneous Provinces: Continental, Oceanic and Planetary Flood Volcanism.* Geophys. Monogr., 100:96–122.

Sullivan, K.D., and Keen, C.E., 1977. Newfoundland Seamounts—petrology and geochemistry. *In* Baragar, W.R.A., Coleman, L.C., and Hall, J.M. (Eds), *Volcanic Regimes of Canada.* Geol. Assoc. Can. Spec. Pap., 16:461–476.

Tarduno, J.A., and Cottrell, R.D., 1997. Paleomagnetic evidence for motion of the Hawaiian hotspot during formation of the Emperor Seamounts. *Earth Planet. Sci. Lett.,* 153(3–4):171–180. doi:10.1016/S0012-821X(97)00169-6

Tucholke, B.E., Sawyer, D.S., and Sibuet, J.-C., in press. Breakup of the Newfoundland-Iberia rift. *In* Karner, G., Manatschal, G., and Pinheiro, L. (Eds.), *Imaging, Mapping and Modelling Continental Lithosphere Extension and Breakup.* Geol. Soc. Spec. Publ.

Tucholke, B.E., and Sibuet, J., 2003. ODP Leg 210 drills the Newfoundland margin in the Newfoundland-Iberia non-volcanic rift. *Eos, Trans. Am. Geophys. Union,* 84(46)(Suppl.):T11E-05. (Abstract)

Tucholke, B.E., Sibuet, J.-C., Klaus, A., et al., 2004. *Proc. ODP, Init. Repts.,* 210: College Station, TX (Ocean Drilling Program). doi:10.2973/odp.proc.ir.210.2004

Van Avendonk, H.J.A., Holbrook, W.S., Nunes, G.T., Shillington, D.J., Tucholke, B.E., Louden, K.E., Larsen, H.C., and Hopper, J.R., 2006. Seismic velocity structure of the rifted margin of the eastern Grand Banks of Newfoundland, Canada. *J. Geophys. Res.,* 111(B11):B11404. doi:10.1029/2005JB004156

Van der Voo, R., 1993. *Paleomagnetism of the Atlantic, Tethys and Iapetus Oceans:* Cambridge (Cambridge Univ. Press).

Verwey, E.J., Haayman, P.W., and Romeijn, F.C., 1947. Physical properties and cation arrangements of oxides with spinal structures, II. Electronic conductivity. *J. Chem. Phys.,* 15(4):181–187. doi:10.1063/1.1746466

Vogt, P.R., 1975. Changes in geomagnetic reversal frequency at times of tectonic change: evidence for coupling between core and upper mantle processes. *Earth Planet. Sci. Lett.,* 25(3):313–321. **doi:10.1016/0012-821X(75)90247-2**

Whitmarsh, R.B., Sawyer, D.S., Klaus, A., and Masson, D.G. (Eds.), 1996. *Proc. ODP, Sci. Results,* 149: College Station, TX (Ocean Drilling Program). **doi:10.2973/odp.proc.sr.149.1996**

Zhao, X., 2001. Paleomagnetic and rock magnetic results from serpentinized peridotites beneath the Iberia Abyssal Plain. *In* Wilson, R.C.L., Whitmarsh, R.B., Taylor, B., and Froitzheim, N. (Eds.), *Non-volcanic Rifting of Continental Margins: A Comparison of Evidence From Land and Sea.* Geol. Soc. Spec. Publ., 187:209–234.

Zhao, X., Roperch, P., and Stokking, L.B., 1994. Magnetostratigraphy of the North Aoba Basin. *In* Greene, H.G., Collot, J.-Y., Stokking, L.B., et al., *Proc. ODP, Sci. Results,* 134: College Station, TX (Ocean Drilling Program), 457–474. **doi:10.2973/odp.proc.sr.134.025.1994**

Zijderveld, J.D.A., 1967. AC demagnetization of rocks: analysis of results. *In* Collinson, D.W., Creer, K.M., and Runcorn, S.K. (Eds.), *Methods in Palaeomagnetism:* New York (Elsevier), 254–286.

Figure F1. Bathymetric map of the North Atlantic Ocean showing locations of Sites 1276 and 1277 in the Newfoundland Basin and Deep Sea Drilling Project and ODP drill sites on the western and southern margins of Galicia Bank on the conjugate Iberia margin (Legs 47B, 103, 149, and 173). Modified from Tucholke, Sibuet, Klaus, et al. (2004).
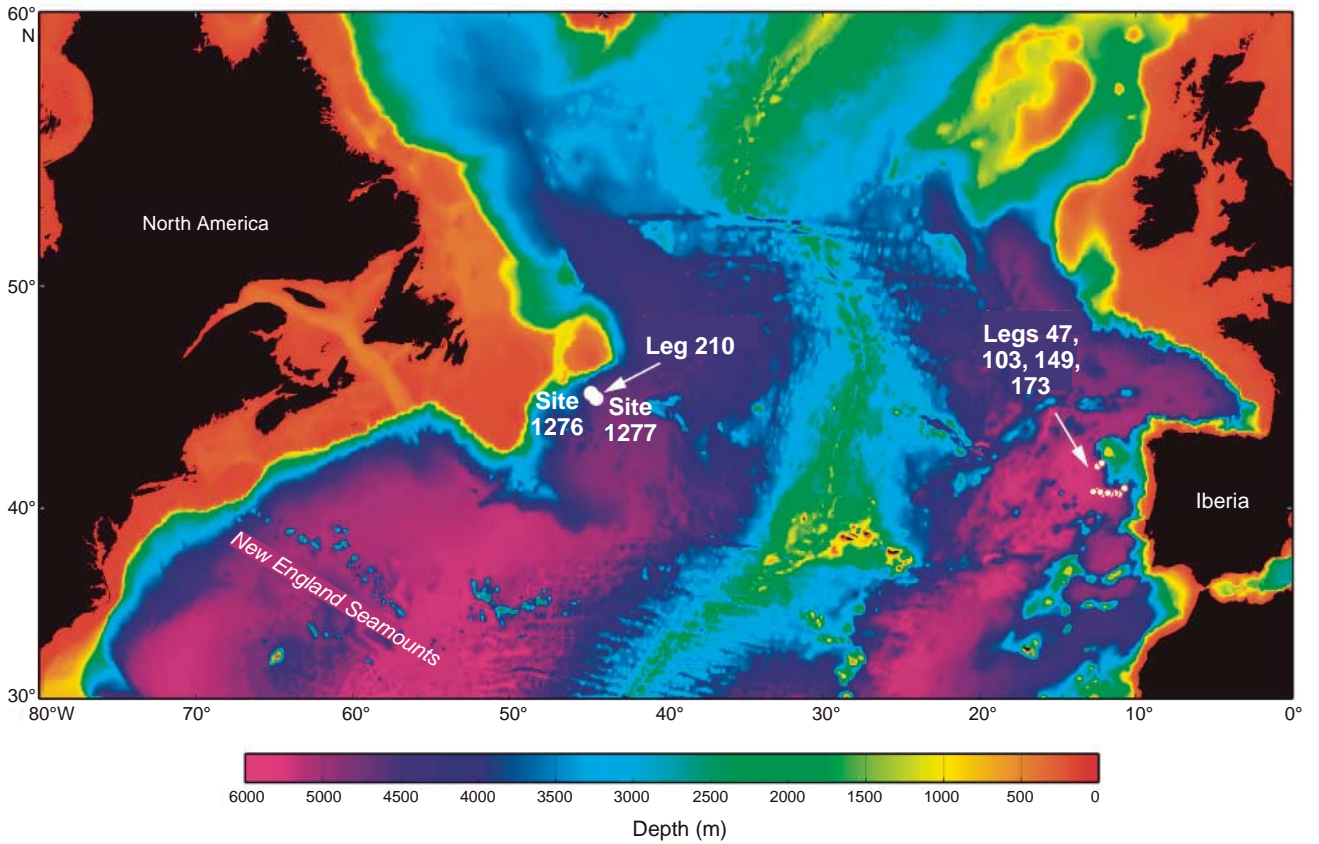
Figure F2. Representative vector endpoint diagrams (Zijderveld, 1967) showing the results of AF demagnetization for split-core samples from just above the sill of Subunit 5C1. **A.** Sample 210-1276A-87R-6, 62 cm, from marble. **B.** Sample 210-1276A-87R-6, 72 cm, from sediments contacting the chilled margin of the upper diabase sill. The baked sedimentary rock has the same ChRM inclination in both samples. Open squares = vector endpoints projected onto the vertical plane, solid squares = vector endpoints projected onto the horizontal plane. NRM = natural remanent magnetization.
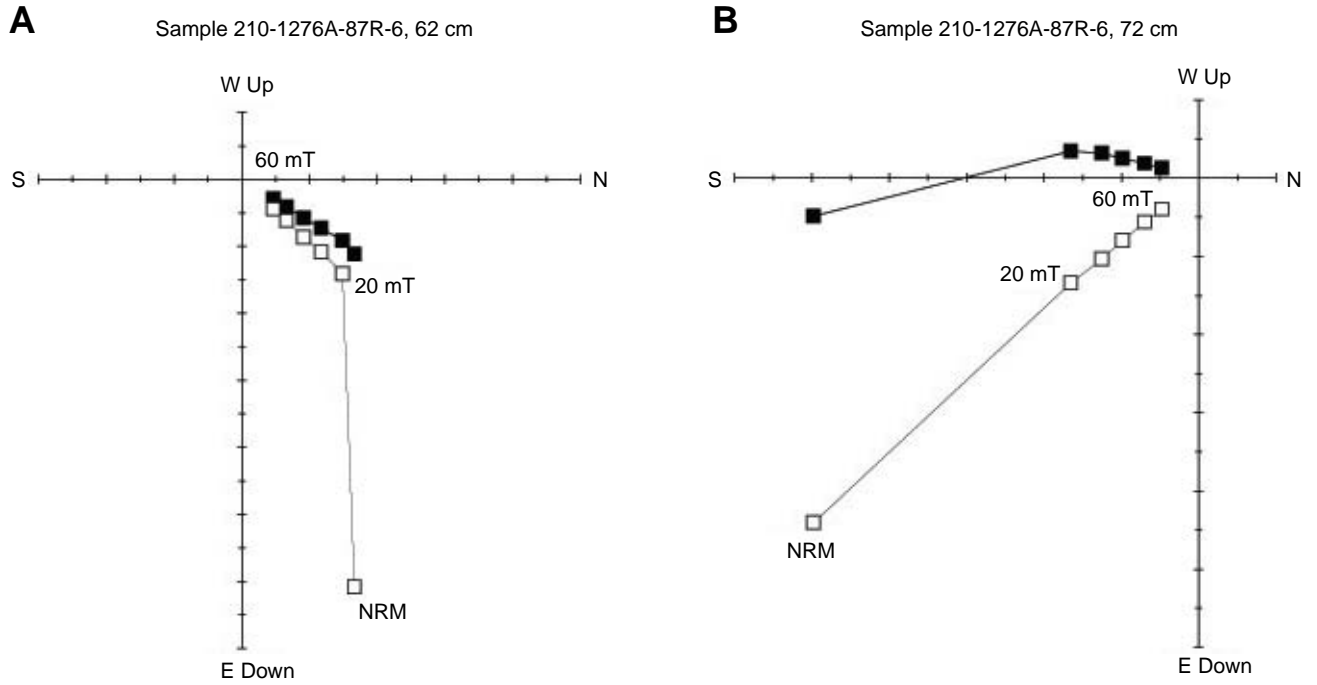
Figure F3. Representative vector endpoint diagrams (Zijderveld, 1967) showing the results of AF demagnetization for diabase sills. **A.** Sample 210-1276A-88R-4, 60 cm, from the upper sill. **B.** Sample 210-1276A-99R-1, 125 cm, from the lower sill. Open squares = vector endpoints projected onto the vertical plane, solid squares = vector endpoints projected onto the horizontal plane. NRM = natural remanent magnetization.
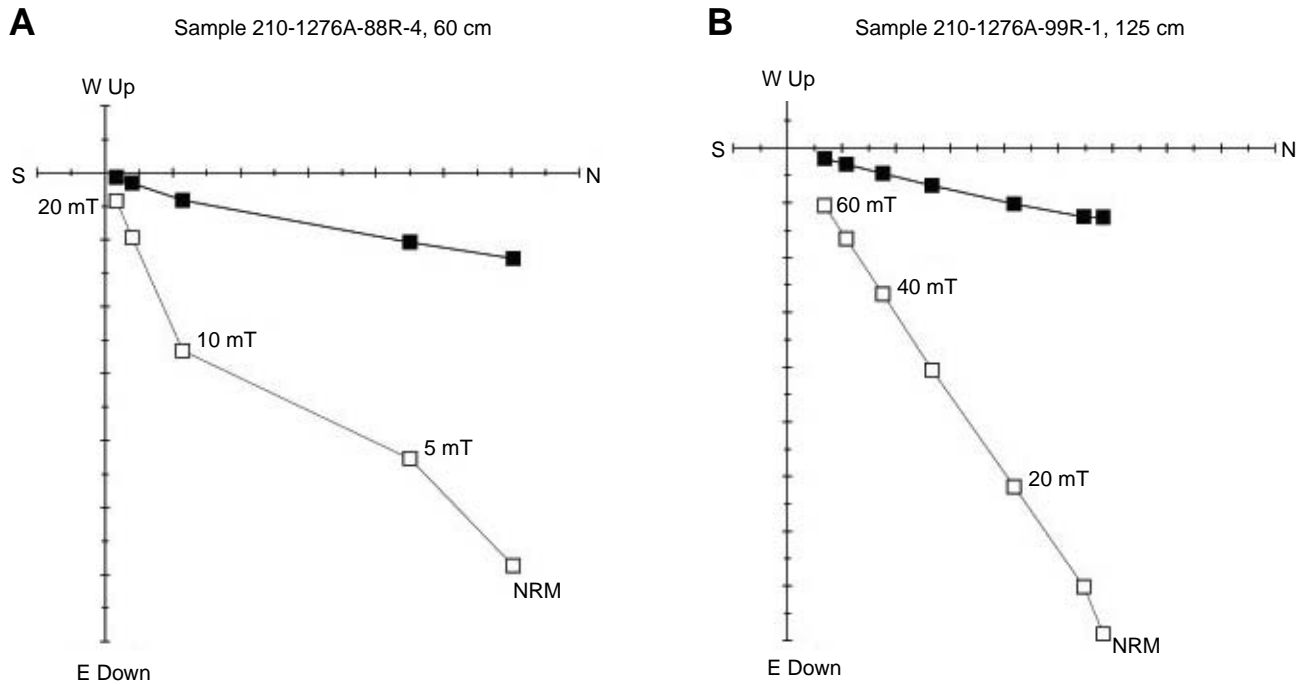
Figure F4. Examples of vector endpoint diagrams for samples from different lithologic units during AF and thermal demagnetization, demonstrating the removal of a normal component of magnetization either caused by drilling or a present geomagnetic field overprint, as well as the isolation of a more stable component that is univectorially decaying toward the origin of the vector plots. **A.** Sample 210-1276A-29R-1, 127–129 cm, from Unit 4. **B.** Black shale Sample 210-1276A-36R-5, 125–127 cm, from Subunit 5B. **C.** Sample 210-1276A-79R-2, 57–59 cm, from Subunit 5C. Open squares = vector endpoints projected onto the vertical plane, solid squares = vector endpoints projected onto the horizontal plane. NRM = natural remanent magnetization.
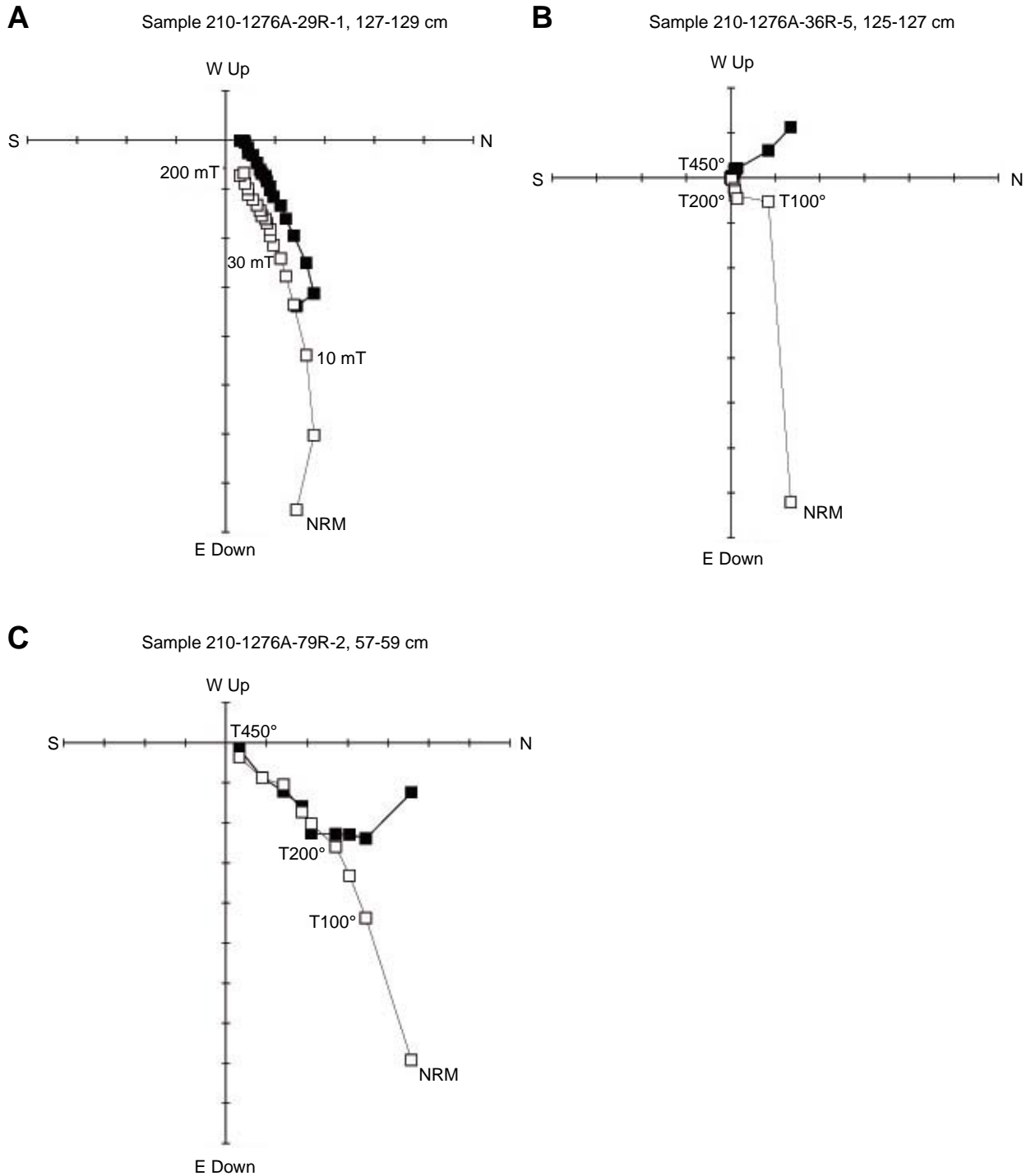
Figure F5. Downhole variation in characteristic remanent magnetization (ChRM) inclinations for rocks and sediments from Site 1276. Open squares = inclinations of the minicore samples, crosses = inclinations of the split-core samples. Lithologic units and expected Cretaceous inclination for the site are also shown.
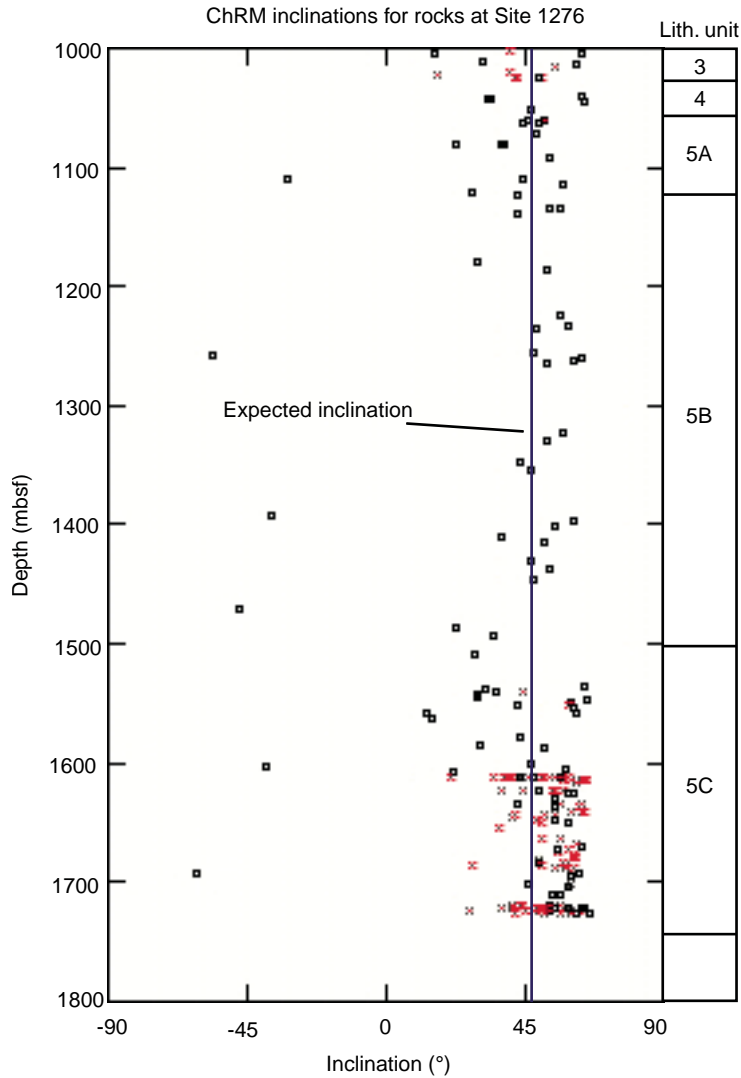
Figure F6. Downhole variation in characteristic remanent magnetization (ChRM) inclinations for rocks from Site 1277. Open squares = inclinations of the minicore samples, crosses = inclinations of the split-core samples. Lithologic units and expected Cretaceous inclination for the site are also shown.
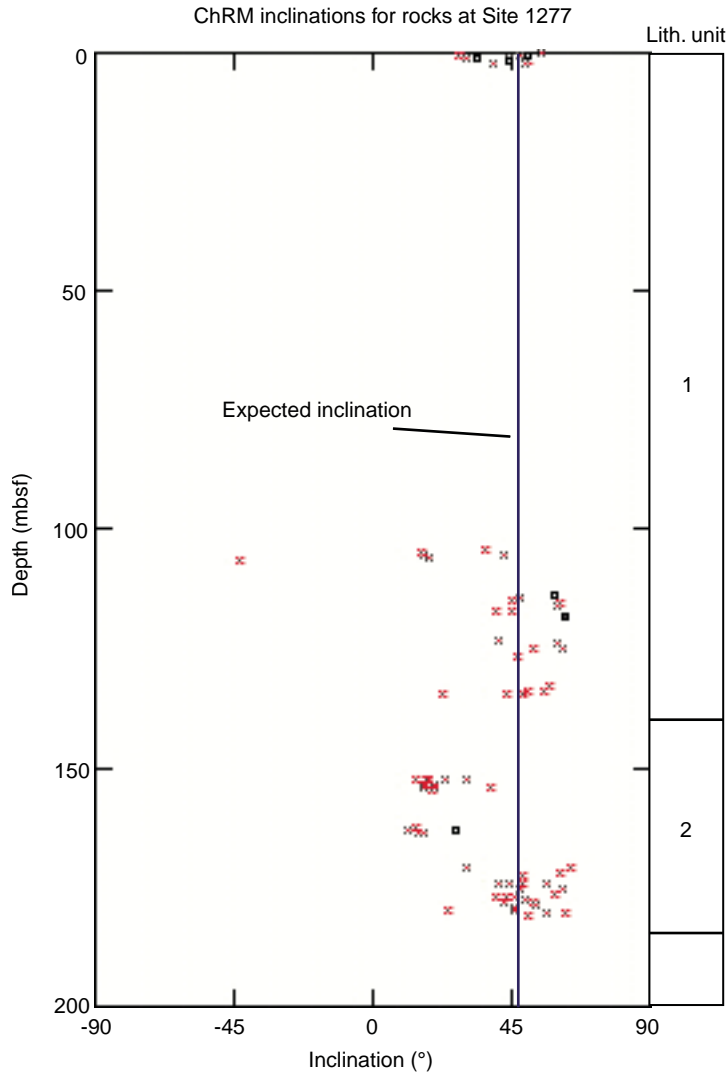
Figure F7. Temperature dependence of magnetization curves for representative (**A**) brown dunite and (**C**) dark-colored serpentinized peridotite. Low-temperature thermal demagnetization of saturation isothermal remanent magnetization (SIRM) acquired at 10 K (red circles) and cooling curve of SIRM acquired at 300 K (blue circles) for (**B**) brown dunite and (**D**) serpentinized peridotite. Arrows show the heating and cooling directions.
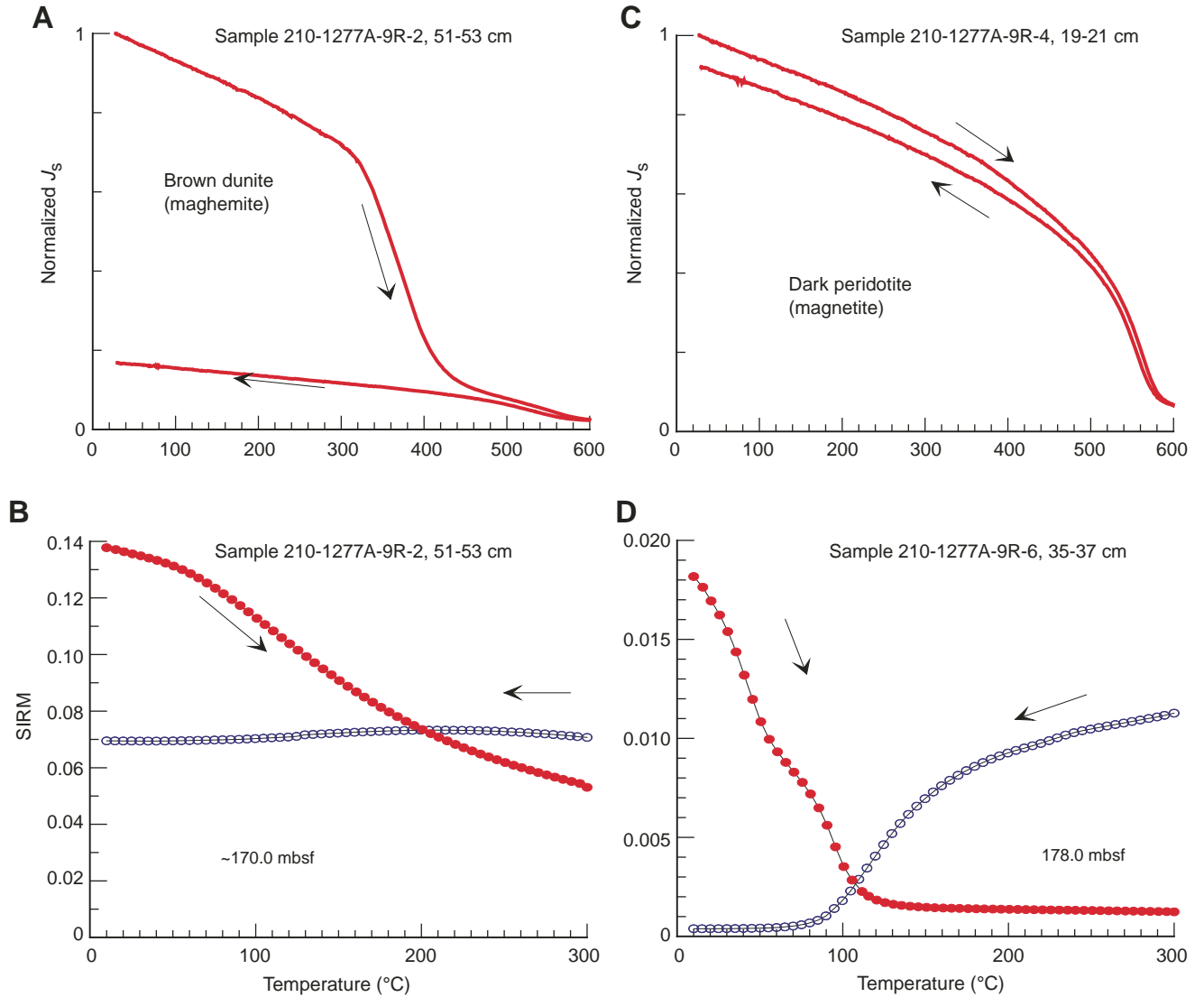
Figure F8. Hysteresis ratios plotted on a Day-type diagram (Day et al., 1977; Dunlop, 2002) for igneous samples from Site 1277. The darker and light ellipsoids mark serpentinized peridotite and overlying basalt samples, respectively. J_s = saturation magnetization, J_r = saturation remanent magnetization, H_c = coercivity, H_{cr} = remanent coercive force. The plot is usually divided into regions: SD = single domain (for $J_s/J_r > 0.5$ and $H_{cr}/H_c < 1.5$), MD = multidomain (for $J_s/J_r < 0.05$ and $H_{cr}/H_c > 4$), PSD = pseudosingle domain (in between SD and MD, SP = super paramagnetic.
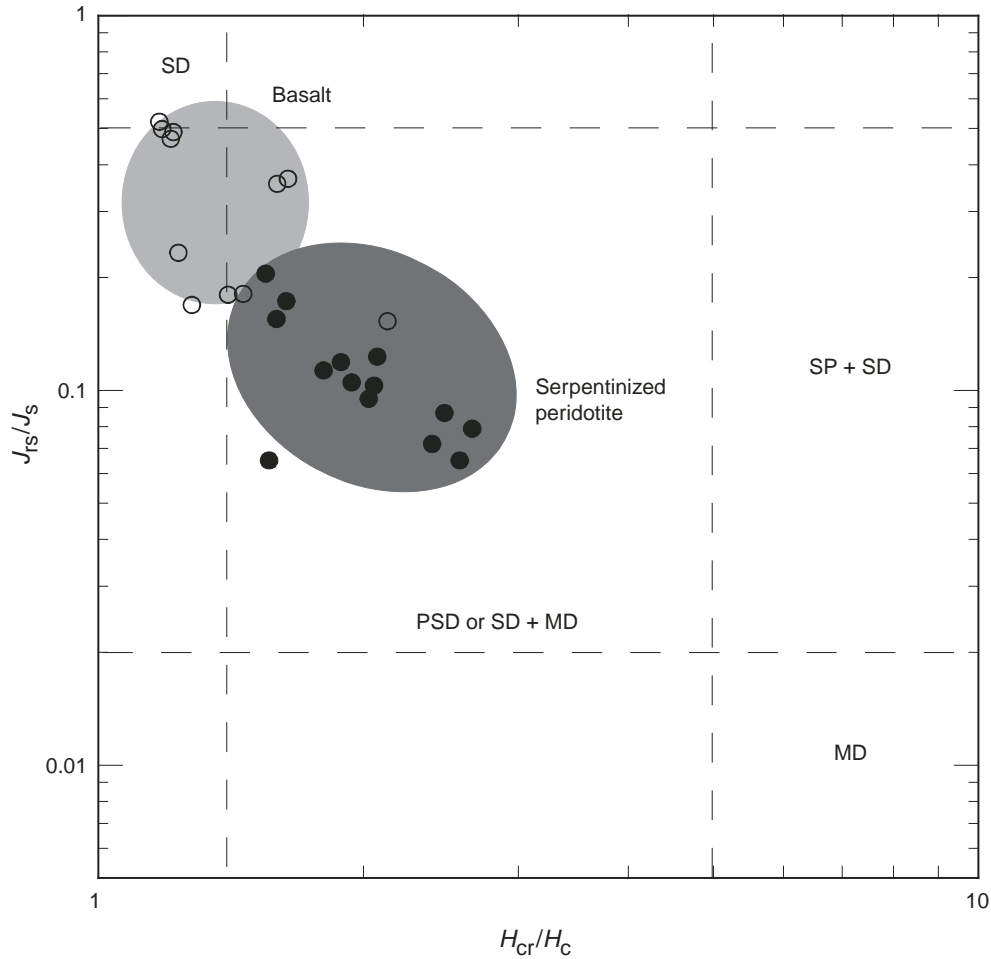
Figure F9. Leg 210 drill Sites 1276 and 1277 (star) and their corresponding paleocolatitudes (small circles), with 95% confidence interval (dark and light gray areas, respectively). Also shown are the Cretaceous paleomagnetic poles of North America and their 95% confidence intervals (data from Table **T4,** p. 36).
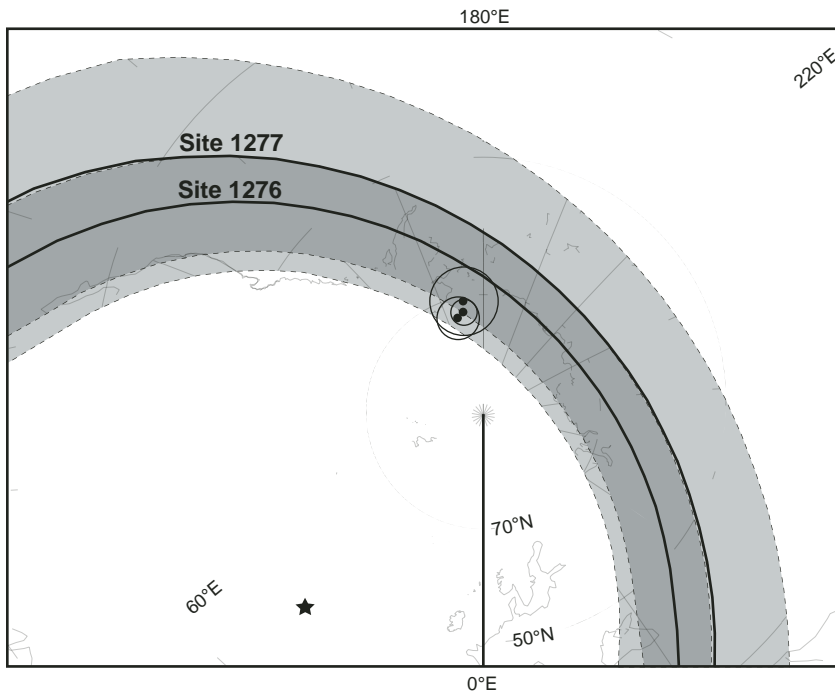
Table T1. Summary of paleomagnetic data of Cretaceous sedimentary and igneous rocks from Leg 210. (**See table notes.** Continued on next five pages.)

Core, section, interval (cm)	Depth (mbsf)	Demagnetization type	Declination (°)	Inclination (°)	Intensity (A/m)	MAD (°)	Sample type
210-1276A-							
23R-1, 78	1002.78	AF	287.2	39.8	1.67E–01	2.2	Split core
23R-3, 24–26	1005.10	AF	323.9	63.5	1.66E–01	4.4	Minicore
23R-4, 61–63	1005.56	AF	284.4	15.2	4.72E–03	4.2	Minicore
24R-1, 45–47	1012.06	Ther	73.4	30.9	1.85E–03	10.9	Minicore
24R-2,128–130	1014.38	AF	27.3	61.3	7.26E–04	6.4	Minicore
24R-4, 8	1016.18	AF	329.6	54.3	6.60E–03	0.4	Split core
24R-4, 59–61	1016.69	Ther	Unstable				Minicore
25R-1, 10	1021.30	AF	193	39.8	1.61E–02	2.3	Split core
25R-1, 88	1022.08	AF	75.3	16.7	1.93E–02	1.6	Split core
25R-3, 6	1024.26	AF	357.4	42.5	2.74E–03	1.5	Split core
25R-3, 28	1024.48	AF	24.9	41.4	7.59E–03	1.8	Split core
25R-3, 38	1024.58	AF	317.7	50.6	1.00E–02	1.2	Split core
25R-4, 2–4	1025.73	AF	131.8	49.6	4.89E–04	5.1	Minicore
25R-5, 67–69	1027.88	Ther	130.6	82.4	1.97E–02	6.3	Minicore
25R-7, 15–17	1029.85	AF	82.9	82.3	1.12E–01	7.3	Minicore
26R-1, 78–80	1031.59	Ther	155.1	87.2	5.41E–03	10	Minicore
26R-2, 50–52	1032.76	Ther	Unstable				Minicore
27R-1, 140–142	1040.91	Ther	292.5	63	5.18E–03	11.9	Minicore
27R-2, 135	1043.30	AF	211.8	33.2	3.34E–02		Split core
27R-2, 135–137	1043.30	AF	200.6	34	3.30E–03	6.8	Minicore
27R-4, 116	1046.07	AF	299.5	51.2	9.83E–03	0.6	Minicore
27R-4, 143–145	1045.34	Ther	252.8	63.8	2.43E–03	8.8	Minicore
27R-6, 136–138	1048.25	Ther	332.5	71	9.44E–03	7.7	Minicore
28R-1, 103–105	1050.54	Ther	259.7	82.7	1.45E–02	7.4	Minicore
28R-1, 103–105	1050.54	AF	195.2	26.1	1.45E–02	4.4	Minicore
28R-2, 102–104	1052.63	AF	116.4	46.8	5.13E–03	10.5	Minicore
28R-4, 99–101	1055.25	Ther	50.1	84.5	1.24E–02	5.6	Minicore
28R-5, 48–50	1056.19	Ther	Unstable				Minicore
29R-1, 2	1059.72	AF	235	51.5	1.50E–02	0.8	Split core
29R-1, 127–129	1060.98	AF	60.1	46.1	8.40E–03	3.6	Minicore
29R-2, 57–59	1061.73	AF	268.5	49.3	1.15E–02	6.7	Minicore
29R-3, 12–14	1062.66	AF	174.6	44.1	4.92E–03	3.1	Minicore
29R-4, 68–70	1064.73	AF	253.6	74.3	1.45E–01	3	Minicore
30R-2, 63–65	1071.42	AF	338.5	48.3	1.07E–03	14.1	Minicore
30R-4, 31–33	1073.95	Ther	223.5	85	1.38E–03	12.9	Minicore
31R-1, 71–73	1079.72	AF	119.8	38.1	8.16E–04	6.4	Minicore
31R-2, 3–5	1080.53	AF	299.9	36.9	9.94E–04	4.2	Minicore
32R-2, 7–9	1080.57	AF	–22.4	22.7	9.90E–04	3.3	Minicore
32R-3, 44–46	1092.05	AF	184.8	53.1	4.17E–04	1.7	Minicore
32R-4, 53–55	1093.42	AF	125.7	78	6.78E–04	1.8	Minicore
32R-5, 97–99	1095.41	AF	165.6	25.3	1.31E–03	3.9	Minicore
33R-1, 143–145	1099.64	AF	246.1	26.1	8.07E–04	3.9	Minicore
33R-5, 39–41	1104.60	Ther	Unstable				Minicore
34R-1, 123–125	1109.04	AF	322.1	–32.3	1.26E–03	10	Minicore
34R-2, 139–141	1110.59	AF	47.8	44.4	1.08E–03	3.5	Minicore
34R-5, 33–35	1113.37	Ther	61.9	56.9	3.40E–03	11.5	Minicore
35R-3, 93–95	1121.33	AF	69.2	28	1.57E–03	13	Minicore
35R-4, 134–136	1123.10	AF	303	42.6	2.71E–03	4.6	Minicore
36R-5, 125–127	1133.83	Ther	–58.5	53.2	7.43E–01	3.7	Minicore
36R-6, 40–42	1134.53	AF	31.4	56.5	4.87E–01	1.6	Minicore
37R-1, 96–98	1137.37	AF	17.3	65.8	5.89E–04	10.1	Minicore
37R-2, 72–74	1138.56	Ther	300	42.2	1.63E–03	16.1	Minicore
38R-2, 45–47	1147.79	AF	301.7	71.9	8.83E–04	4.5	Minicore
39R-2, 38–40	1157.05	AF	188.3	44.5	3.54E–04	3.9	Minicore
40R-2, 26–28	1166.57	Ther	Unstable				Minicore
41R-4, 33–35	1179.24	AF	163.7	29.3	1.13E–03	2.7	Minicore
42R-2, 53–55	1185.79	AF	12.7	52	5.08E–04	3.5	Minicore
43R-3, 21–23	1196.67	Ther	345.1	64.8	7.65E–04	4.3	Minicore
45R-1, 17–19	1212.98	AF	327.5	46.6	4.94E–04	2.6	Minicore
46R-1, 95–97	1223.36	AF	305.1	56.5	5.91E–04	2.5	Minicore
47R-1, 8–10	1232.09	Ther	133.3	59.1	5.64E–03	3.9	Minicore
47R-2, 61–63	1234.12	Ther	182.3	73.8	1.29E–03	6.1	Minicore
47R-3, 49–51	1235.53	AF	208.2	48.6	1.23E–03	4.4	Minicore
49R-4, 119–121	1256.10	AF	232.6	47.5	8.20E–04	3.8	Minicore
49R-5, 126–128	1257.67	AF	142	–56.5	7.84E–04	1.1	Minicore
49R-6, 94–96	1259.85	AF	291	63.3	9.77E–04	7.2	Minicore
50R-2, 69–71	1263.20	AF	280.4	60.6	1.59E–03	7.4	Minicore

Table T1 (continued).

Core, section, interval (cm)	Depth (mbsf)	Demagnetization type	Declination (°)	Inclination (°)	Intensity (A/m)	MAD (°)	Sample type
50R-4, 5–7	1265.56	AF	17	51.7	2.96E–03	6	Minicore
53R-3, 109–111	1294.10	AF	253.3	74.3	6.45E–04	3.9	Minicore
54R-3, 137–139	1303.98	AF	163.1	68.6	1.90E–03	3.3	Minicore
55R-2, 80–82	1311.51	Ther	Unstable				Minicore
56R-1, 89–91	1319.70	AF	111.8	77.6	3.01E–03	6.4	Minicore
56R-3, 34–36	1322.14	AF	59.7	57.3	3.41E–03	3.5	Minicore
57R-1, 86–88	1329.37	AF	61.3	51.7	1.04E–03	5.7	Minicore
59R-2, 147–149	1347.08	AF	287.5	43.5	2.09E–03	5	Minicore
59R-5, 35–37	1350.46	Ther	Unstable				Minicore
59R-7, 51–53	1353.12	AF	331.6	46.5	1.20E–03	2.7	Minicore
64R-1, 21–23	1392.41	AF	108.3	–37.3	9.52E–03	13.7	Minicore
64R-4, 139–141	1397.10	Ther	296	60.8	2.94E–03	10.7	Minicore
65R-1, 12–14	1401.93	AF	145	54.6	1.25E–03	12.6	Minicore
65R-6, 100–102	1410.31	AF	124.8	37	8.78E–04	11.6	Minicore
66R-2, 76–78	1413.57	AF	12.2	51	9.93E–04	8.4	Minicore
67R-5, 101–103	1427.92	AF	44.5	–70.3	9.41E–04	8.3	Minicore
67R-7, 37–39	1429.78	AF	245.3	46.8	1.67E–03	3.3	Minicore
68R-4, 104–106	1436.04	Ther	207.1	53.1	2.66E–03	5.7	Minicore
69R-5, 16–18	1445.96	AF	167.6	47.3	1.18E–03	5.3	Minicore
72R-2, 54–56	1470.95	AF	242.9	–47.6	1.79E–03	5.6	Minicore
73R-6, 56–58	1486.57	AF	209.1	22.8	3.53E–03	1.7	Minicore
74R-4, 133–135	1493.94	AF	23.6	34.5	2.57E–03	2.2	Minicore
76R-2, 49–51	1509.30	Ther	343	28.9	6.15E–03	6.5	Minicore
76R-4, 116–118	1512.97	Ther	Unstable				Minicore
76R-7, 36–38	1516.47	Ther	Unstable				Minicore
77R-4, 31–33	1521.72	Ther	Unstable				Minicore
78R-6, 121–123	1535.21	Ther	288.8	64.4	2.67E–03	14.2	Minicore
79R-2, 5–7	1537.76	Ther	42.5	31.7	2.77E–03	7.3	Minicore
79R-3, 44	1539.64	AF	1.8	43.9	1.34E–03	1.8	Split core
79R-3, 86–88	1540.06	Ther	105.6	35.3	6.34E–03	6.1	Minicore
79R-5, 70–72	1542.91	AF	101.1	29.1	1.51E–03	6.8	Minicore
79R-6, 36–38	1544.07	AF	357.7	29.6	1.47E–03	4.4	Minicore
80R-1, 117–119	1546.98	AF	54.8	64.8	8.86E–04	2.7	Minicore
80R-3, 102–104	1549.83	AF	189.3	59.6	3.04E–03	6.1	Minicore
80R-4, 80	1551.10	AF	356.3	58.8	4.10E–03	0.6	Split core
80R-5, 12–14	1551.93	Ther	206.7	42.1	2.10E–03	10.2	Minicore
80R-6, 33–35	1553.14	Ther	209.5	60.3	2.08E–03	3.1	Minicore
81R-1, 38–40	1557.79	Ther	202.3	13	4.05E–03	4.9	Minicore
81R-3, 6–8	1558.47	AF	345.4	61.9	2.62E–03	3.1	Minicore
81R-3, 99–101	1559.40	AF	8.5	66.6	3.73E–03	1.3	Minicore
81R-5, 66–68	1561.90	Ther	201.8	14.6	3.68E–03	6.1	Minicore
83R-3, 57–59	1578.07	Ther	178.6	43.3	2.84E–03	1.2	Minicore
84R-1, 23–25	1584.43	Ther	–0.7	30.2	7.00E–03	2	Minicore
84R-1, 100–102	1585.21	AF	342.8	73	6.39E–03	1.8	Minicore
85R-1, 47–49	1588.18	AF	4.7	50.9	2.48E–03	1.7	Minicore
86R-5, 94–96	1601.75	AF	238.8	47.2	4.46E–03	1.3	Minicore
86R-6, 20–22	1602.01	AF	342.5	–39.1	5.21E–03	2.4	Minicore
87R-1, 17–19	1604.68	AF	314.6	57.6	2.02E–03	2.9	Minicore
87R-2, 135–137	1606.36	AF	191.6	21.3	2.28E–03	3.3	Minicore
87R-5, 138–140	1610.89	AF	162.1	48	4.80E–03	1.8	Minicore
87R-6, 0	1612.11	AF	343.3	40.7	2.60E–03	2.2	Split core
87R-6, 8	1612.19	AF	299.8	58.9	4.68E–03	3.3	Split core
87R-6, 20	1612.31	AF	–40	52.8	3.38E–03	1.7	Split core
87R-6, 24	1612.35	AF	–40.1	54.8	3.40E–03	0.7	Split core
87R-6, 30	1612.41	AF	–43.1	48.4	3.98E–03	0.6	Split core
87R-6, 40	1612.51	AF	317.4	40	4.46E–03	0.7	Split core
87R-6, 46	1612.57	AF	163.3	39.3	4.39E–03	0.9	Split core
87R-6, 50	1612.61	AF	157.7	20.8	4.95E–03	0.3	Split core
87R-6, 60	1612.71	AF	21	45.7	5.53E–03	0.5	Split core
87R-6, 62	1612.73	AF	31.9	38.7	6.41E–03	0.4	Split core
87R-6, 66	1612.77	AF	47.9	56.2	7.46E–03	0.6	Split core
87R-6 (Piece 2A, 69–71)	1612.80	AF	48	56.2	7.46E–03	0.6	Minicore
87R-6, 70	1612.81	AF	189.2	50.4	1.05E–02	0.9	Split core
87R-6, 72	1612.83	AF	193.2	38.5	1.33E–02	1.1	Split core
87R-6, 74	1612.83	AF	195.3	35	1.67E–02	1.8	Split core
87R-6 (Piece 4A, 80–82)	1612.91	AF	297	43	5.76E–02	1.9	Split core
87R-6 (Piece 4A, 82)	1612.93	AF	291.2	42.9	9.60E–02	2.4	Split core
87R-6 (Piece 4A, 84)	1612.95	AF	247.5	51.4	1.48E–01	13.8	Split core
87R-6 (Piece 4A, 86)	1612.97	AF	–88.3	52.4	2.01E–01	5.4	Split core

Table T1 (continued).

Core, section, interval (cm)	Depth (mbsf)	Demagnetization type	Declination (°)	Inclination (°)	Intensity (A/m)	MAD (°)	Sample type
87R-6 (Piece 4A, 88)	1612.99	AF	−83.8	64.6	2.84E−01	5.6	Split core
87R-6 (Piece 5A, 90)	1613.01	AF	−36.3	72.7	6.42E−01	0.4	Split core
87R-6 (Piece 5A, 92)	1613.03	AF	−5.6	63.3	1.37E+00	2.2	Split core
87R-6 (Piece 5A, 112)	1613.23	AF	50.8	86.8	2.84E+00	1.4	Split core
87R-6 (Piece 6A, 132)	1613.43	AF	169.1	74.3	2.80E+00	1.7	Split core
87R-7 (Piece 1A, 2)	1613.53	AF	34.4	75.3	2.13E+00	1.2	Split core
87R-7 (Piece 1A, 12)	1613.63	AF	194.7	59.7	1.64E+00	0.6	Split core
87R-7 (Piece 2A, 18)	1613.69	AF	3.7	57.2	2.37E+00	1.4	Split core
88R-1 (Piece 2A, 4)	1614.14	AF	27.7	64.5	2.47E+00	2.5	Split core
88R-1 (Piece 2A, 58)	1614.68	AF	125.8	64.8	2.08E+00	3	Split core
88R-1, 94–96	1615.05	AF	162.2	77	1.11E−01	1.8	Minicore
88R-2 (Piece 1A, 26)	1615.38	AF	108	74.8	3.47E+00	0.9	Split core
88R-2 (Piece 1B, 55–57)	1615.66	AF	285.7	76.8	4.84E+00	2.1	Minicore
88R-2 (Piece 3A, 80)	1615.92	AF	8.4	73.5	3.68E+00	0.7	Split core
88R-2 (Piece 4B, 114)	1616.26	AF	216.4	70.2	3.87E+00	1.5	Split core
88R-2 (Piece 5A, 122)	1616.34	AF	−24.8	61.2	3.74E+00	1.4	Split core
88R-2 (Piece 6A, 140)	1616.52	AF	193.4	68	2.81E+00	2.8	Split core
88R-3 (Piece 2A, 22)	1616.78	AF	179.9	71.8	3.63E+00	2	Split core
88R-3 (Piece 5A, 42)	1616.98	AF	356.2	68.2	5.41E+00	1.8	Split core
88R-3 (Piece 6A, 56)	1617.12	AF	67.5	74.9	3.35E+00	2.1	Split core
88R-3 (Piece 7A, 72)	1617.28	AF	37.3	76.8	5.37E+00	1.3	Split core
88R-3 (Piece 8A, 92)	1617.48	AF	348.6	74.9	5.51E+00	0.7	Split core
88R-3 (Piece 9A, 106)	1617.62	AF	19.6	70.5	5.67E+00	1.7	Split core
88R-3 (Piece 10A, 120)	1617.76	AF	288.1	71.2	4.47E+00	2.4	Split core
88R-3 (Piece 11A, 134)	1617.90	AF	349.8	72.9	5.58E+00	1.7	Split core
88R-3 (Piece 12A, 142)	1617.98	AF	30	86.2	3.43E+00	1.8	Split core
88R-4 (Piece 1A, 8)	1618.14	AF	−61.6	72.1	4.24E+00	2.2	Split core
88R-4 (Piece 2A, 28)	1618.34	AF	59	82.3	3.59E+00	2.2	Split core
88R-4 (Piece 8A, 60)	1618.66	AF	19.9	65.4	1.70E+00	0.3	Split core
88R-4 (Piece 9A, 80)	1618.86	AF	304.1	70.7	3.78E+00	2	Split core
88R-4 (Piece 10A, 100)	1619.06	AF	151	83.2	4.04E+00	2	Split core
88R-4 (Piece 11A, 122)	1619.28	AF	319.4	73.2	4.66E+00	2	Split core
88R-4 (Piece 12A, 142)	1619.48	AF	201.3	82.1	3.65E+00	2.2	Split core
88R-5 (Piece 1A, 8)	1619.61	AF	54.5	79.1	4.39E+00	1.7	Split core
88R-5 (Piece 1B, 22)	1619.75	AF	60.9	76.7	5.45E+00	1.8	Split core
88R-5 (Piece 2A, 38)	1619.91	AF	312.7	80.2	5.35E+00	2.1	Split core
88R-5 (Piece 3A, 60)	1620.13	AF	36	77.4	5.59E+00	2.1	Split core
88R-5 (Piece 3B, 90)	1620.43	AF	50.7	81.1	4.53E+00	1.3	Split core
88R-6 (Piece 1A, 42)	1621.04	AF	74.9	86.1	3.73E+00	0.9	Split core
88R-6 (Piece 1A, 60–62)	1621.23	AF	292.7	78.7	5.20E+00	1.5	Minicore
88R-6 (Piece 2A, 78)	1621.40	AF	91.2	82.9	3.34E+00	1.6	Split core
88R-6 (Piece 3A, 102)	1621.64	AF	150.6	79.2	3.02E+00	0.6	Split core
88R-7 (Piece 1A, 9)	1621.92	AF	211.8	81.8	3.71E+00	0.9	Split core
88R-7 (Piece 2A, 48)	1622.31	AF	85.9	80.3	3.79E+00	2	Split core
88R-7 (Piece 3A, 84)	1622.67	AF	52.1	73	3.39E+00	1.6	Split core
88R-7 (Piece 5A, 111)	1622.94	AF	84.4	75.5	2.34E+00	0.4	Split core
88R-8, 20	1623.24	AF	0.7	57.2	1.70E−03	3.3	Split core
88R-8, 32	1623.36	AF	13.5	54.5	1.21E−03	3.7	Split core
88R-8, 46–48	1623.52	AF	12.3	49.7	2.85E−03	1.7	Minicore
88R-8, 50	1623.54	AF	168.5	44.6	2.14E−03	1.3	Split core
88R-8, 80	1623.84	AF	254.5	53.7	3.34E−03	2.3	Split core
88R-8, 90	1623.94	AF	−35.5	54.2	3.30E−03	6.3	Split core
89R-1, 12	1623.72	AF	131.9	37.2	2.77E−03	2.6	Split core
89R-1, 54	1624.14	AF	28.9	44.5	2.43E−03	2.5	Split core
89R-2, 104–106	1625.15	AF	216.8	60.6	5.69E−03	1.4	Minicore
89R-2, 119–121	1626.30	AF	128.6	58.8	2.17E−03	3	Minicore
89R-5, 132–134	1629.98	AF	86.3	54.3	1.61E−03	5.8	Minicore
90R-1, 17–19	1633.48	AF	30.5	42.4	1.91E−03	4	Minicore
90R-2, 2	1634.82	AF	23.6	56	1.46E−03	2.1	Split core
90R-2, 50	1635.30	AF	−33.9	63.5	1.68E−03	3.3	Split core
90R-3, 54	1636.81	AF	−66.8	62.7	1.82E−03	1.1	Split core
90R-3, 128–130	1637.59	AF	52.2	54.5	1.54E−03	4.2	Minicore
90R-4, 92–94	1638.73	AF	81	−69.9	2.11E−03	7.2	Minicore
90R-5, 124	1640.51	AF	−2.5	59.4	2.52E−03	6.3	Split core
90R-6, 38	1641.15	AF	−77.3	63.8	1.93E−03	2.4	Split core
90R-6, 74	1641.51	AF	−30.4	63	6.49E−03	4.8	Split core
90R-6, 84–86	1641.65	AF	99	75.3	1.60E−03	5.7	Minicore
90R-7, 56	1642.23	AF	56.7	51.3	5.35E−03	4	Split core
91R-1, 20	1643.00	AF	108.7	42	1.25E−03	1.9	Split core

Table T1 (continued).

Core, section, interval (cm)	Depth (mbsf)	Demagnetization type	Declination (°)	Inclination (°)	Intensity (A/m)	MAD (°)	Sample type
91R-1, 68	1643.48	AF	228.2	54.6	5.31E–03	3.7	Split core
91R-2, 50–52	1644.81	AF	115.8	70.2	2.09E–03	3.9	Minicore
91R-2, 96	1645.26	AF	58	40.3	1.47E–03	2.1	Split core
91R-3, 102	1646.82	AF	198.6	48.1	2.41E–03	9.3	Split core
91R-3, 123–125	1647.04	AF	351.6	54.8	4.20E–03	2.8	Minicore
91R-4, 109–111	1647.40	Ther	54.6	65.5	1.46E–03	5.2	Minicore
91R-5, 22	1649.02	AF	–42.9	50.3	8.89E–04	3.2	Split core
91R-5, 30–32	1649.11	AF	52.1	58.8	1.09E–03	8.5	Minicore
91R-5, 60	1649.40	AF	125.6	66	1.44E–03	1.5	Split core
92R-1, 118	1653.68	AF	302.5	36	3.82E–03	8.6	Minicore
92R-3, 142–144	1656.93	AF	38.5	66.5	2.04E–03	6.8	Minicore
92R-CC, 49–51	1661.48	AF	265.5	83.1	2.82E–03	9.1	Minicore
93R-1, 82	1662.92	AF	91.2	50.2	2.88E–03	4	Split core
93R-2, 24	1663.84	AF	10.1	56.7	3.26E–03	2.9	Split core
93R-4, 76	1667.36	AF	64.9	61.2	1.07E–02	3	Split core
93R-5, 99–101	1669.10	AF	56.3	63.2	2.57E–03	1.6	Minicore
94R-1, 20–22	1672.01	AF	320.6	55.7	4.42E–03	2.8	Minicore
94R-1, 20	1672.01	AF	132.1	58.6	3.55E–03	0.7	Split core
94R-1, 78	1672.58	AF	128.1	65.6	2.98E–03	3.9	Split core
94R-3, 92	1675.57	AF	27.5	55.1	4.53E–03	3.9	Split core
94R-5, 30	1677.89	AF	0.4	60.7	1.62E–02	2	Split core
94R-5, 76	1678.35	AF	237.3	60.5	4.30E–03	1.9	Split core
94R-5, 106	1678.65	AF	225.4	61.5	3.75E–03	1.4	Split core
94R-6, 67–69	1679.78	AF	250	66.7	3.22E–03	3	Minicore
95R-1, 26	1681.66	AF	3.8	49.4	9.57E–03	9.5	Split core
95R-2, 54	1683.10	AF	176.7	57	1.46E–03	0.5	Split core
95R-3, 5–7	1684.12	AF	306.1	49.6	1.66E–03	5.8	Minicore
95R-3, 74	1684.80	AF	146	50.6	4.97E–03	1.6	Split core
95R-3, 108	1685.14	AF	240.7	57.9	1.77E–03	4	Split core
95R-3, 150	1685.56	AF	288.6	28	3.09E–04	3.4	Split core
95R-5, 24	1687.20	AF	8.2	60.9	7.94E–04	1.8	Split core
95R-5, 34	1687.30	AF	18.3	58.1	8.02E–04	2.5	Split core
95R-5, 130	1688.26	AF	102.1	54.5	1.02E–03	1.3	Split core
96R-1, 18	1691.08	AF	135.5	71.8	3.56E–03	0.5	Split core
96R-1, 55–57	1691.46	AF	96.2	62.1	3.94E–03	7.9	Minicore
96R-1, 80	1691.70	AF	–17.6	69.3	3.18E–03	1.6	Split core
96R-2, 78–80	1693.12	AF	187.6	–61.6	4.07E–03	2.7	Minicore
96R-3, 136–138	1695.20	AF	179.4	59.8	4.42E–03	2.7	Minicore
97R-1, 24	1700.74	AF	133.2	59.8	3.72E–03	2.6	Split core
97R-1, 94–96	1701.45	AF	119.2	45.6	5.13E–04	5.5	Minicore
97R-2, 86–88	1702.86	AF	85.9	59.2	4.24E–04	0.5	Minicore
98R-1, 38	1710.48	AF	–13.9	66.9	8.64E–04	0.9	Split core
98R-1, 100–102	1711.10	AF	–5.2	53.7	6.93E–04	2.9	Minicore
98R-1, 120–122	1711.31	AF	83	56.1	8.59E–03	9.5	Minicore
99R-1 (Piece 4A, 20)	1719.60	AF	221.3	44.1	1.66E–01	0.1	Split core
99R-1 (Piece 9A, 44)	1719.84	AF	69.1	43.4	1.12E–01	0.3	Split core
99R-1 (Piece 18A, 86)	1720.26	AF	49.3	40.4	1.43E–01	0.7	Split core
99R-1 (Piece 18A, 87–89)	1720.28	AF	216.9	52.9	2.97E–01	0.9	Minicore
99R-1 (Piece 18A, 90)	1720.31	AF	24.9	56	1.39E–01	0.2	Split core
99R-1 (Piece 18A, 94)	1720.34	AF	12.6	74.8	9.47E–02	0.2	Split core
99R-1, 99–101	1720.39	AF	53.6	57.2	4.14E–03	0.4	Minicore
99R-1 (Piece 19A, 104)	1720.44	AF	68.8	52.5	1.46E–01	0.3	Split core
99R-1 (Piece 20A, 117–119)	1720.58	AF	202.8	62.8	2.92E–01	0.4	Minicore
99R-1 (Piece 21A, 126)	1720.66	AF	14.7	55.8	2.14E–01	0.2	Split core
99R-2 (Piece 1A, 6)	1720.89	AF	153.6	52.2	1.41E–01	0.3	Split core
99R-2 (Piece 3A, 22)	1721.05	AF	192.7	40.4	1.15E–01	0.3	Split core
99R-2 (Piece 5A, 36)	1721.19	AF	269.7	49.9	1.78E–01	0.2	Split core
99R-2 (Piece 8A, 49–51)	1721.33	AF	340.7	54.5	2.99E–01	0.7	Minicore
99R-2 (Piece 8A, 56)	1721.39	AF	161.4	54	1.70E–01	0.1	Split core
99R-2 (Piece 10A, 76)	1721.59	AF	118.7	48.4	1.78E–01	0.2	Split core
99R-2 (Piece 11A, 86–88)	1721.69	AF	85.9	59.2	4.84E–01	0.5	Minicore
99R-2 (Piece 11A, 86)	1721.69	AF	265	37	4.84E–01	0.4	Split core
99R-2 (Piece 18A, 136)	1722.19	AF	99.4	48.8	1.65E–01	0.3	Split core
99R-3 (Piece 1A, 8)	1722.37	AF	183.5	58.5	1.56E–01	1.1	Split core
99R-3, 13–15	1722.43	AF	344.3	63.9	2.50E–01	0.8	Minicore
99R-3 (Piece 2A, 26)	1722.55	AF	273.4	49.4	1.63E–01	0.3	Split core
99R-3 (Piece 4A, 46)	1722.75	AF	147.3	48.7	2.14E–01	0.6	Split core
99R-3 (Piece 8A, 72)	1723.01	AF	120	50.1	2.07E–01	0.4	Split core
99R-3, 83–85	1723.12	AF	119.7	–4.8	1.39E–01	0.3	Minicore

Table T1 (continued).

Core, section, interval (cm)	Depth (mbsf)	Demagnetization type	Declination (°)	Inclination (°)	Intensity (A/m)	MAD (°)	Sample type
99R-3 (Piece 10A, 94)	1723.23	AF	224.6	44.7	2.09E–01	0.1	Split core
99R-3 (Piece 11A, 106)	1723.35	AF	355.7	27	2.22E–01	0.4	Split core
99R-3 (Piece 12A, 116)	1723.45	AF	–89.5	49.8	1.99E–01	0.4	Split core
99R-3 (Piece 13A, 126)	1723.55	AF	36.8	52.2	1.80E–01	0.3	Split core
99R-3 (Piece 14A, 140)	1723.69	AF	230.8	49.8	2.06E–01	0.3	Split core
99R-3 (Piece 14A, 148)	1723.77	AF	215.7	50.3	8.95E–02	0.2	Split core
99R-5 (Piece 1A, 2)	1723.98	AF	7.6	50.4	1.34E+00	2.9	Split core
99R-5, 26	1724.22	AF	4	61.8	3.21E+00	2.2	Split core
99R-5, 27–29	1724.24	AF	142	52.6	3.72E+00	1	Minicore
99R-5 (Piece 1B, 34)	1724.30	AF	–46.4	6	3.42E+00	4.9	Split core
99R-5 (Piece 1C, 38)	1724.34	AF	–38.6	63.8	3.18E+00	3.8	Split core
99R-5 (Piece 2A, 56)	1724.52	AF	124	59.8	3.85E–01	1.8	Split core
99R-5, 90	1724.86	AF	182.5	47.3	8.76E–01	2.1	Split core
99R-5, 110	1725.06	AF	–56.6	50.8	2.78E+00	3.9	Split core
99R-5, 111–113	1725.08	AF	109.5	61.5	3.51E+00	0.6	Minicore
99R-6 (Piece 1A, 4)	1725.20	AF	70.2	41.3	3.44E–01	2.3	Split core
99R-6, 10–12	1725.27	AF	42.4	65.9	5.57E+00	1.2	Minicore
99R-6, 14	1725.30	AF	267.3	59.8	2.50E+00	5.6	Split core
99R-6, 18	1725.34	AF	–77.7	65.7	3.16E+00	4.9	Split core
99R-6, 26	1725.42	AF	246.9	55.9	2.81E+00	4.4	Split core
210-1277A-							
1W-1, 24	0.25*	AF	318.17	54.28	5.25E–01	3.3	Split core
1W-1 (Piece 6A, 48)	0.49*	AF	–60.8	47.4	5.57E–01	4.7	Split core
1W-1 (Piece 6A, 56)	0.57*	AF	181.5	27.7	4.41E–01	3.1	Split core
1W-1 (Piece 8A, 83–85)	0.74*	AF	162.6	50.5	3.51E–03	2.7	Minicore
1W-1 (Piece 9A, 102)	1.03*	AF	245.4	44.2	2.97E+00	2.1	Split core
1W-1 (Piece 10A, 108)	1.09*	AF	28.58	44.51	1.35E+00	1.6	Split core
1W-1 (Piece 10A, 110)	1.11*	AF	32.5	30.4	2.39E+00	1.6	Split core
1W-1 (Piece 11A, 118–120)	1.19*	AF	218	33.8	3.68E–03	2.6	Minicore
1W-2 (Piece 1A, 6–8)	1.43*	AF	127.4	44.5	1.96E–03	4.9	Minicore
1W-2 (Piece 1B, 28)	1.65*	AF	–53.1	50.3	3.42E+00	2.4	Split core
1W-2 (Piece 6A, 94)	2.31*	AF	186.1	49	2.37E–01	7.6	Split core
1W-2 (Piece 6A, 100)	2.37*	AF	202.1	38.8	4.28E–01	2.7	Split core
2R-1 (Piece 4A, 28)	104.19	AF	–9.22	36.39	6.92E–01	0.9	Split core
2R-1 (Piece 12A, 114)	105.05	AF	137.3	15.49	2.16E–01	0.8	Split core
2R-1 (Piece 12A, 116)	105.07	AF	148	16.2	2.07E–01	0.5	Split core
2R-2 (Piece 3A, 26)	105.56	AF	140.2	42.7	5.47E–02	0.6	Split core
2R-2 (Piece 9A, 62)	105.92	AF	92.2	18.6	2.59E–02	1.7	Split core
2R-2 (Piece 18A, 102)	106.32	AF	137.1	–43.2	7.23E–01	2.2	Split core
2R-2 (Piece 18A, 116)	106.46	AF	115.6	–42.9	6.42E–01	4.1	Split core
3R-1 (Piece 1B, 6–8)	113.67	AF	18.1	59.3	1.47E–03	0.7	Minicore
3R-1 (Piece 9A, 80)	114.41	AF	127	47.4	1.62E+00	4	Split core
3R-1 (Piece 10A, 100)	114.61	AF	–25.3	45	1.35E+00	3.5	Split core
3R-2 (Piece 6A, 44)	115.46	AF	111.6	60.4	5.26E–01	4.1	Split core
3R-2 (Piece 12A, 116)	116.18	AF	163.6	59.9	6.27E–01	5.7	Split core
3R-3 (Piece 5A, 50)	117.02	AF	257.6	45	1.23E+00	2.5	Split core
3R-3 (Piece 5B, 54)	117.06	AF	240.9	40	1.03E+00	2	Split core
3R-3 (Piece 13A, 128)	117.80	AF	142.6	75.4	2.55E+00	1.5	Split core
3R-4 (Piece 1A, 2–4)	117.99	AF	354.1	62.2	2.03E–03	0.9	Minicore
3R-4 (Piece 1A, 10)	118.07	AF	190.4	62.6	2.31E+00	2.6	Split core
3R-4 (Piece 2A, 34)	118.31	AF	–31.4	70.6	2.31E+00	2	Split core
4R-1 (Piece 3A, 18)	123.19	AF	198	40.7	1.10E+00	2.6	Split core
4R-1 (Piece 4A, 66)	123.67	AF	130.6	59.6	5.27E+00	6.3	Split core
4R-1 (Piece 11A, 140)	124.41	AF	218.8	–0.9	2.36E–04	1.4	Minicore
4R-2 (Piece 5A, 35)	124.80	AF	307.9	61.3	8.64E–06	1.4	Split core
4R-2 (Piece 6A, 50)	124.95	AF	190.9	51.9	1.98E–01	1.3	Split core
4R-3 (Piece 1A, 6)	126.61	AF	5.1	46.5	1.80E+00	0.6	Split core
5R-1 (Piece 2A, 12)	132.73	AF	146.5	57.5	1.79E+00	2.7	Split core
5R-1 (Piece 6A, 88)	133.49	AF	206.6	67.6	1.56E+00	1	Split core
5R-2 (Piece 1A, 4)	134.08	AF	39.9	50	5.35E–01	3.6	Split core
5R-2 (Piece 2A, 10)	134.14	AF	353.29	55.52	1.56E–01	1.1	Split core
5R-2 (Piece 2A, 12)	134.16	AF	285.06	–4.2	1.55E–01	1.7	Split core
5R-2 (Piece 4A, 24)	134.28	AF	61.31	48.41	2.39E–01	5.5	Split core
5R-2 (Piece 5A, 30)	134.34	AF	79.93	42.97	6.98E–01	3.5	Split core
5R-2 (Piece 9A, 66)	134.70	AF	193.75	22.66	1.07E+00	1.7	Split core
5R-3 (Piece 9A, 57–59)	136.10	AF	22.7	–3.1	4.74E+00	1.3	Minicore
6R-1 (Piece 13B, 98)	143.09	AF	206.4	7.2	1.35E+00	2.3	Split core
7R-1 (Piece 11A, 50)	152.31	AF	8.7	18.5	2.65E+00	4.4	Split core
7R-1 (Piece 11B, 56)	152.37	AF	318.86	23.41	2.25E+00	2.4	Split core

Table T1 (continued).

Core, section, interval (cm)	Depth (mbsf)	Demagnetization type	Declination (°)	Inclination (°)	Intensity (A/m)	MAD (°)	Sample type
7R-1 (Piece 11C, 64)	152.45	AF	240.73	30.28	1.33E+00	6.6	Split core
7R-1 (Piece 13A, 80)	152.61	AF	253.6	17.1	8.05E–01	3.5	Split core
7R-1 (Piece 13A, 82)	152.63	AF	255.03	13.62	1.23E+00	2.8	Split core
7R-1 (Piece 18A, 110)	152.91	AF	323.3	9.14	1.53E+00	1.6	Split core
7R-2 (Piece 1B, 16)	153.40	AF	247.42	16.7	1.34E+00	2.3	Split core
7R-2 (Piece 4B, 46)	153.70	AF	278.16	19.6	8.56E–01	1.5	Split core
7R-2 (Piece 5A, 58)	153.82	AF	245.13	16.58	1.53E–01	1	Split core
7R-2 (Piece 8A, 74)	153.98	AF	179.63	19.65	4.10E–01	1.4	Split core
7R-2 (Piece 9A, 90)	154.14	AF	306.27	38.06	2.08E–01	7.4	Split core
7R-2 (Piece 12A, 118)	154.42	AF	324.58	19.22	2.32E–01	0.2	Split core
8R-1 (Piece 15A, 78)	162.29	AF	350.17	–1.71	8.91E–02	0.4	Split core
8R-1 (Piece 20A, 112)	162.63	AF	119.98	9.54	1.39E+00	3.4	Split core
8R-1 (Piece 21A, 124)	162.75	AF	272.2	13.59	1.56E+00	1.4	Split core
8R-1 (Piece 21A, 128–130)	162.79	AF	75.6	27	1.74E–03	5.4	Minicore
8R-1 (Piece 22A, 144)	162.95	AF	301.85	2.34	2.34E–02	0.4	Split core
8R-2 (Piece 2A, 26)	163.22	AF	151.87	11.21	1.49E+00	1.1	Split core
8R-2 (Piece 2A, 30)	163.26	AF	322.4	8	1.22E–03	3.9	Split core
8R-2 (Piece 2B, 42)	163.38	AF	148.16	16.59	8.32E–01	0.4	Split core
8R-2 (Piece 2B, 46)	163.42	AF	153.9	14.38	5.13E–01	0.3	Split core
8R-2 (Piece 2B, 48)	163.44	AF	165.13	16.24	3.49E–01	0.6	Split core
9R-1 (Piece 1A, 18)	170.89	AF	320.12	64.26	2.30E–01	1.5	Split core
9R-1 (Piece 2A, 33)	171.04	AF	151.2	30	6.56E–04	2.2	Split core
9R-1 (Piece 2F, 129)	171.96	AF	152.5	60.3	2.40E–04	3.4	Split core
9R-2 (Piece 2A, 51)	172.71	AF	109.1	48.1	1.38E–03	1.1	Split core
9R-3 (Piece 2A, 30)	173.98	AF	151.51	56.32	4.03E+00	1.9	Split core
9R-3 (Piece 3E, 64)	174.32	AF	308.67	40.45	1.55E+00	1.7	Split core
9R-3 (Piece 3E, 70)	174.38	AF	303.49	48.51	1.21E+00	1.2	Split core
9R-3 (Piece 3E, 76)	174.44	AF	335.55	44.21	2.88E+00	5.9	Split core
9R-3 (Piece 3G, 99)	174.67	AF	145.1	68.4	7.34E–03	2.1	Split core
9R-3 (Piece 3H, 120)	174.88	AF	331.07	69.08	4.69E+00	6.9	Split core
9R-4 (Piece 1A, 19)	175.21	AF	146.4	61.5	2.47E–03	4.4	Split core
9R-4 (Piece 1D, 50)	175.52	AF	341.44	65.69	2.54E+00	10.3	Split core
9R-4 (Piece 1E, 62)	175.64	AF	340.05	47.8	1.90E+00	4.3	Split core
9R-4 (Piece 1G, 120)	176.22	AF	324.75	59.04	3.65E+00	5.2	Split core
9R-4 (Piece 1G, 131)	176.33	AF	95.1	71.7	7.67E–03	2.3	Split core
9R-5 (Piece 1C, 58)	177.01	AF	333.79	46.16	1.40E+00	1.5	Split core
9R-5 (Piece 1D, 66)	177.09	AF	229.22	43.53	4.37E–01	1.8	Split core
9R-5 (Piece 3B, 86)	177.29	AF	323.41	39.73	5.06E–01	0.3	Split core
9R-5 (Piece 3B, 92)	177.35	AF	345.14	49.46	1.21E+00	1.1	Split core
9R-6 (Piece 1A, 10)	177.83	AF	324.19	66.2	3.19E+00	6	Split core
9R-6 (Piece 1B, 36)	178.06	AF	71	42.7	2.26E–03	2.1	Split core
9R-6 (Piece 1B, 44)	178.17	AF	282.83	51.8	1.93E+00	3.4	Split core
9R-6 (Piece 1D, 124)	178.97	AF	285.25	53.21	2.96E+00	5.6	Split core
9R-7 (Piece 1A, 8)	179.17	AF	207.03	45.62	1.61E+00	11.5	Split core
9R-7 (Piece 1B, 28)	179.37	AF	48.5	–6.9	2.08E–03	1.5	Split core
9R-7 (Piece 1F, 66)	179.75	AF	291.19	23.88	2.04E+00	2.8	Split core
9R-7 (Piece 2A, 88)	179.97	AF	305.06	46.06	2.70E+00	4.8	Split core
9R-7 (Piece 3A, 122)	180.31	AF	311.9	69.61	3.02E+00	2.3	Split core
9R-7 (Piece 3A, 125)	180.34	AF	97.8	67.4	4.37E–03	2.5	Split core
9R-8 (Piece 1A, 14)	180.52	AF	319.37	56.2	2.92E+00	2.2	Split core
9R-8 (Piece 1A, 24)	180.62	AF	282.97	62.29	1.49E+00	6.2	Split core
9R-8 (Piece 3A, 40)	180.78	AF	316.56	50.4	1.88E+00	3.2	Split core

Notes: * = distances from core top, not depth. AF = alternating field, Ther = thermal. MAD = maximum angular deviation.

Table T2. Summary of rock magnetic properties of rock samples considered for this study. (**See table notes.** Continued on next page.)

Core, section, interval (cm)	Depth (mbsf)	Rock Type	Alteration	T_c (°C) $[T_{c1}, T_{c2}]$ (Kappabridge)	T_c (°C) $[T_{c1}, T_{c2}]$ (MicroVSM)	T_v (K)	H_c (mT)	H_{cr} (mT)	H_{cr}/H_c	J_r (mAm²/kg)	J_s (mAm²/kg)	J_r/J_s
210-1276A-												
Subunit 5C1, 105 Ma												
87R-6, 86–89	1601.94	Diabase sill	Complete				14.2			2.94	7.69	0.38
87R-6, 90–92	1601.98	Diabase sill	Complete	565		b	23.2	25.8	1.11	1.38	2.78	0.50
87R-6, 108–113	1602.26	Diabase sill	Complete				4.71	13.3	2.82	103	1620	0.06
87R-6, 129–130	1602.47	Diabase sill	Complete				4.82	9.96	2.07	246	3440	0.07
88R-1, 93–95	1605.40	Diabase sill	Moderate		515	125	3.4	7.37	2.17	157	2650	0.06
88R-2, 93–96	1606.43	Diabase sill	Moderate		540	130	3.9	10.5	2.69	41.3	657	0.06
88R-3, 56–59	1608.10	Diabase sill	Moderate		510	128	4.02	8.97	2.23	126	1690	0.07
88R-3, 121–125	1608.75	Diabase sill	Moderate				3.53	8.19	2.32	196	3180	0.06
88R-4, 72–74	1609.76	Diabase sill	Moderate	480		140	3.46	9.2	2.66	94	1630	0.06
88R-4, 110–115	1610.15	Diabase sill	Moderate				3.47	7.79	2.24	173	2620	0.07
88R-5, 104–109	1611.62	Diabase sill	Moderate		515	130	3.82	8.77	2.30	129	1900	0.07
88R-6, 69–72	1612.80	Diabase sill	Moderate			125	3.62	7.88	2.18	164	2470	0.07
88R-7, 39–40	1613.90	Diabase sill	Moderate			120	4	9.69	2.42	168	2590	0.07
88R-7, 93–96	1614.44	Diabase sill	High				4.57	8.77	1.92	226	2700	0.08
Subunit 5C2, 98 Ma												
98R-1, 120–122	1712.30	Diabase sill	Moderate		540	110	3.37	16.5	4.90	1.58	221	0.01
99R-1, 117–119	1720.57	Diabase sill	Moderate			b	29.5	35.2	1.19	0.695	6.44	0.11
99R-1, 123–126	1720.63	Diabase sill	Moderate							0	245	0.00
99R-2, 49–51	1721.32	Diabase sill	Moderate	590	560	b	20.1	34.2	1.70	2.34	10.4	0.23
99R-3, 13–15	1722.42	Diabase sill	Moderate		552	b	24.8	34.1	1.38	2.31	7.53	0.31
99R-3, 110–114	1723.30	Diabase sill	Moderate				22	29.2	1.33	2.96	7.99	0.37
99R-5, 6–8	1724.06	Diabase sill	Moderate	560	580	105	17.2	28.5	1.66	297	1240	0.08
99R-5, 27–29	1724.27	Diabase sill	Moderate				16.5	29.2	1.77	250	1160	0.22
99R-5, 111–113	1725.07	Diabase sill	Moderate				16	29	1.81	127	648	0.20
99R-6, 10–12	1725.26	Diabase sill	Moderate		570		15.1	28.1	1.86	138	705	0.20
210-1277A-												
Unit 1 (Cretaceous?)												
1W-1, 83–86	.83*	Basalt	High			c	6.96	8.58	1.23	81.6	351	0.23
1W-2, 6–8	1.42*	Pillow basalt breccia	High				5.78	7.38	1.28	93.3	552	0.17
2R-1, 97–99	104.87	Basalt	High	640		125	–2.05			0.602	112	0.01
2R-2, 115–117	106.45	Diabase	Moderate				20.5	23.5	1.15	53.6	106	0.51
3R-1, 6–8	114.20	Basalt	High	350, 560	385, 570	c	18	21.9	1.22	69.6	142	0.49
3R-1, 40–42	114.56	Basalt	High				34	42.2	1.24	47.4	82.7	0.57
3R-2, 45–47	115.46	Basalt	High				17.8	32.9	1.85	5.54	32	0.17
3R-2,102–104	116.03	Basalt	High		580	125	15.2	33	2.17	3.58	17	0.21
3R-2, 118–120	116.19	Basalt	High	590	410, 590	120	17.3	20.9	1.21	103	220	0.47
3R-3, 107–109	117.58	Basalt	High		380, 585	x	25.5	29.9	1.17	82.9	159	0.52
3R-4, 1–3	117.96	Basalt	High	390, 580		x	21.5	25.4	1.18	88.7	178	0.50
4R-1, 140–142	124.40	Basalt	High	570	540	b	43.8	71.9	1.64	2.11	5.76	0.37
4R-2, 35–37	124.79	Gabbro			675	130	9.52	15.2	1.60	1.28	3.61	0.36
5R-1, 13–15	132.73	Basalt	High		500, 570	b	6.31	8.86	1.40	35	195	0.18
5R-1, 89–91	133.49	Basalt	High		530, 605		7.19	10.5	1.46	62.3	344	0.18
5R-2, 60–62	134.63	Basalt	High		530, 595	128	10.7	22.8	2.13	70.4	461	0.15
5R-3, 49–51	136.02	Gabbro			590	108	–15.3			0.446	–0.7	0.00

Table T2 (continued).

Core, section, interval (cm)	Depth (mbsf)	Rock Type	Alteration	T_c (°C) $[T_{c1}, T_{c2}]$ (Kappabridge)	$[T_{c1}, T_{c2}]$ (MicroVSM)	T_v (K)	H_c (mT)	H_{cr} (mT)	H_{cr}/H_c	J_r (mAm^2/kg)	J_s (mAm^2/kg)	J_r/J_s
Unit 2 (126 Ma)												
8R-1, 128–130	162.78	Darker peridotite	Serpentinized		560, 620		11.3	17.5	1.55	106	520	0.21
8R-2, 30–32	163.25	Darker peridotite	Serpentinized	410, 585	555	110	11.5	18.8	1.63	202	1170	0.17
9R-1, 33–35	171.00	Brown dunite	Serpentinized		455		7.28	18	2.47	17.8	205	0.09
9R-1, 129–131	171.96	Brown dunite	Serpentinized			c	6.62	17.6	2.66	110	1390	0.08
9R-2, 51–53	172.71	Brown dunite	Serpentinized			c	9.69	20.1	2.07	243	1980	0.12
9R-2, 141–143	173.60	Brown dunite	Serpentinized		625		6.25	9.96	1.59	33.7	218	0.16
9R-3, 99–101	174.66	Darker peridotite	Serpentinized		500, 570	102	5.62	11.4	2.03	140	1470	0.10
9R-4, 19–21	175.20	Darker peridotite	Serpentinized		585		6.29	12.2	1.94	123	1170	0.11
9R-4, 131–133	176.32	Darker peridotite	Serpentinized			110	7.73	15.9	2.06	133	1290	0.10
9R-5, 5–7	176.47	Darker peridotite	Serpentinized	405, 590	560	105	5.89	14.1	2.39	116	1600	0.07
9R-5, 103–106	177.45	Darker peridotite	Serpentinized				9.24	17.4	1.88	73.9	615	0.12
9R-6, 36–38	178.08	Darker peridotite	Serpentinized	400, 595	554	107	5.79	14.9	2.57	86.7	1330	0.07
9R-6, 112–114	178.84	Darker peridotite	Serpentinized		585		8.59	16.2	1.89	93.7	790	0.12
9R-7, 28–31	179.36	Darker peridotite	Serpentinized	400, 590	560	105	11.2	17.5	1.56	162	947	0.07
9R-8, 40–42	180.77	Darker peridotite	Serpentinized		580		7.88	14.2	1.80	132	1170	0.11
9R-8, 43–45	180.80	Darker peridotite	Serpentinized				8.33	14.5	1.74	228	1980	0.12

Notes: * = distances from core top, not depth. The rock type and degrees of alteration are from Tucholke, Sibuet, Klaus, et al. (2004), see text for references. T_c = Curie temperature, T_{c1} = low Curie temperature, T_{c2} = high Curie temperature, VSM = vibrating sample magnetometer. T_v = Verwey transition; b, c, x = groups of low-temperature magnetometry, see text.

Table T3. Mean inclinations and paleolatitudes of Sites 1276 and 1277, Newfoundland Basin.

Description	Depths of samples (mbsf)	Age	N	Mean inclination (°)	α95	k	r	Mean paleolatitude (°)	α95	k	r	F{0.975}
Site 1276 (45°24.3198′N, 44°47.1496′W)												
Unit 4	1040.50–1062.53	Turonian–Santonian	11	46.3	9.5	23.7	10.5776	**28.7**	8.0	33.0	10.6965	f(1,10)~6.94
Subunit 5A	1071.42–1123.1	Cenomanian–Turonian	12	39.5	9.5	21.1	11.4784	**23.3**	7.0	38.1	11.7113	f(1,11)~6.72
Subunit 5B	1133.88–1493.94	Albian–Cenomanian	30	49.5	4.4	33.9	29.1452	**31.2**	3.6	47.7	29.3923	f(1,29)~5.59
Sediments above Sill 1	1508.8–1612.77	Albian	33	43.3	6.3	15.5	30.9287	**26.8**	4.7	25.4	31.7400	f(1,32)~5.54
Sill 1 (Subunit 5C1) and baked sediment	1612.81–1622.94	105 Ma	14	53.5	7.2	30.6	13.5744	**35.2**	6.7	34.5	13.6228	f(1,13)~6.41
Sediments above Sill 2	1623.24–1711.31	Albian–Aptian(?)	55	54.3	2.6	51.9	53.96	**35.5**	2.3	60.3	54.1049	f(1,54)~5.33
Sill 2 (Subunit 5C2)	1719.6–1725.42	98 Ma	38	51.4	3.1	51.7	37.2837	**32.7**	2.7	63.9	37.4212	f(1,37)~5.47
Subunit 5C	1508.8–1725.42	Albian–Aptian(?)	140	50.4	3.4	17.6	132.115	**32.2**	2.2	27.4	134.9189	f(1,139)~5.11
Subunit 5C	1508.8–1725.42	Albian–Aptian(?)	4*	47.3	16.7	51.8	3.942	**28.9**	13.9	74.5	3.9597	f(1,3)~17.44
Subunits 5B and 5C	1133.88–1725.42	Cenomanian–Aptian(?)	5	47.7	10.9	67.6	4.9408	**29.2**	9.1	98.0	4.9592	f(1,4)~12.22
Subunit 5	1071.42–1725.42	Turonian–Aptian(?)	6	46.4	9.2	65.5	5.9236	**29.0**	7.6	95.4	5.9476	f(1,5)~10.01
Mean A	1040.5–1725.4	Santonian–Aptian(?)	193	49.4	2.8	19.0	182.898	**31.3**	1.8	29.2	186.4347	f(1,192)~4.99
Mean B	1040.5–1725.4	Santonian–Aptian(?)	7†	*46.3*	7.3	78.6	6.9237	***30.3***	5.1	162.6	6.9631	f(1,6)~8.81
Site 1277 (45°11.8002′N, 44°22.5999′W)												
Unit 1	104.19–136.1	Cretaceous?	27‡	45.8	6.8	16.6	25.4322	**28.64**	5.0	27.8	26.07	f(1,26)~5.66
		Cretaceous?	39	44.9	5	20.8	37.1755	**27.65**	3.7	34.7	37.905	f(1,38)~5.45
Unit 2	143.09–180.78	126 Ma	41	36.67	6.7	11.4	37.4873	**22.11**	4.5	21.9	39.1742	f(1,40)~5.42
	143.09–180.78	126 Ma	34**	39.6	7.3	11.4	31.1004	**24.2**	5.1	21.6	32.4748	f(1,33)~5.53
Units 1 and 2‡, **	104.19–180.78	Cretaceous–126 Ma	61	42.4	5.3	12.9	56.3523	**26.1**	3.6	23.5	58.451	f(1,60)~5.29
Units 1 and 2 (All samples)	104.19–180.78	Cretaceous–126 Ma	80	40.7	4.5	13.7	74.2399	**24.9**	3.0	25.4	76.8952	f(1,79)~5.25
Units 1 and 2 (Core means‡)	104.19–180.78	Cretaceous–126 Ma	7	*38.5*	17.6	13.8	6.5664	***22.9***	12.0	29.0	6.7933	f(1,6)~8.81

Note: * = average of Subunit 5C1 (Sills 1), Subunit 5C2 (Sill 2) and two sediment intervals within Subunit 5C; † = average of Unit 4, Subunits 5A and 5B, and 4 intervals within Subunit 5C; ‡ = omitted samples in Core 1W; ** = omitted dark dunite samples. Age = approximate age estimates from shipboard biostratigraphic studies and post-cruise Ar-Ar isotopic dating (see text for references), N = number of samples or units, α95 = radius of circle of 95% confidence, k = estimated precision parameter, r = resultant vector, F{0.975} = F-statistics at 97.5% confidence. Mean inclination calculated by the method of McFadden and Reid (1982). Italics = used for Table T4, p. 36, bold = paleolatitude estimates.

Table T4. Summary of paleolatitudes obtained from this study and inferred from mid-Cretaceous paleomagnetic poles for North America, Europe, and the Avalon Terrane.

Age range	P_{lat} (°)	P_{long} (°)	$\alpha 95$ (°)	Paleolat (°)	Source of data
Laurentia (combined N. America-Greenland)					
125 Ma	70.5	192.5	3.5	33.0 ± 3.1	Besse and Courtillot (2002)
120 Ma	71.2	194.2	3.1	33.9 ± 2.7	Besse and Courtillot (2002)
100 Ma	76.4	197.7	0.4	38.0 ± 5.1	Besse and Courtillot (2002)
90 Ma	75.3	196.4	3.5	37.1 ± 2.8	Besse and Courtillot (2002)
90–125 Ma	73.4	194.9	3.4	**35.2 ± 2.8**	Average of above 4, this study
97–130 Ma	72.7	191.1	2.1	**34.2 ± 1.8**	McElhinny and McFadden (1999)
98–144 Ma	71.0	190.0	5.4	**32.8 ± 4.8**	Van der Voo (1993)
Europe					
125 Ma	75.7	192.4	3.5	36.6 ± 2.9	Besse and Courtillot (2002)
120 Ma	76.5	193.5	3.1	37.3 ± 2.5	Besse and Courtillot (2002)
100 Ma	85.1	144.5	11.5	40.6 ± 8.8	Besse and Courtillot (2002)
90 Ma	80.8	185.8	3.5	39.2 ± 2.7	Besse and Courtillot (2002)
90–125 Ma	79.9	186.1	6.1	**38.4 ± 3.8**	Average of above 4, this study
97–146 Ma	70.5	206.5	7.3	**36.6 ± 6.0**	McElhinny and McFadden (1999)
98–144 Ma	76.0	194.0	5.0	**36.5 ± 4.1**	Van der Voo (1993)
Avalon Terrane (= Avalon Peninsula of eastern Newfoundland)					
67–97 Ma	73.0	193.0	9.7	**35.3 ± 8.3**	Van der Voo (1993)
115–144 Ma	67.0	212.0	4.0	**35.7 ± 3.3**	Van der Voo (1993)
Newfoundland Basin					
Santonian–Aptian (84–125 Ma)				**30.3 ± 5.1**	This study
Lower Cretaceous–126 Ma				**22.9 ± 12.0**	This study

Notes: P_{lat} = north latitude of paleomagnetic pole positions, P_{long} = east longitude of paleomagnetic pole position, $\alpha 95$ = radius of circle of 95% confidence about the pole position in degrees, Paleolat = paleolatitudes of Sites 1276 and 1277 calculated from the corresponding paleomagnetic pole position. Bold = paleolatitude estimates.

CHAPTER NOTE*

N1. Jagoutz, O., Muntener, O., Manatschal, G., Rubatto, D., Peron-Pinvidic, G., Turrin, B.D., and Villa, I.M., submitted. The rift-to-drift transition in the southern North Atlantic: a stuttering start for the MORB engine? *Geology.*